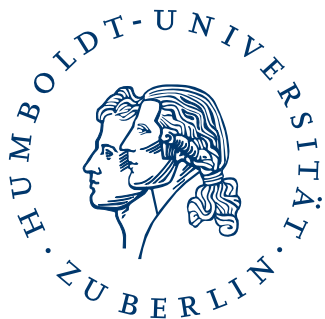


Kohärente Spinmanipulation am Stickstofffehlstellenzentrum in Diamant

MASTERARBEIT

zur Erlangung des akademischen Grades

Master of Science
im Fach Physik



eingereicht an der
Mathemetisch-Naturwissenschaftlichen Fakultät I
Institut für Physik
Humboldt-Universität zu Berlin

von
Stefan Maximilian Strauß

Gutachter:

1. Prof. Dr. Oliver Benson
2. Prof. Dr. Stefan Kowarik

eingereicht am: 31. Oktober 2013

Zusammenfassung

In der vorliegenden Arbeit untersuchen wir experimentell Eigenschaften des Stickstofffehlstellenzentrum in Diamant und weisen insbesondere den Quantzenoeffekt nach. Dies stellt die erste experimentelle Untersuchung dieses Effektes an einem Einzelsystem dar.

Auf Grund seiner einzigartigen Merkmale hat sich das Stickstofffehlstellenzentrum als geeignetes System für vielerlei Experimente und Anwendungen im Bereich der Quantenoptik und darüber hinaus erwiesen. Die Grundtechnik, welche in dieser Arbeit zum Einsatz kommt, ist die optische Detektion magnetischer Resonanz. Wir benutzen diese um den Elektron спин einzelner Stickstofffehlstellenzentren kohärent zu manipulieren und so Phänomene wie Rabi-Oszillationen und Spinechos zu messen. Hauptziel unserer Untersuchungen ist der Quantzenoeffekt. Dieses Phänomen rein quantenmechanischer Natur beschreibt die Unterbindung kohärenter zeitlicher Entwicklung durch wiederholte Messungen. Wir zeigen dieses Phänomen experimentell an einzelnen Stickstofffehlstellenzentren und gewinnen so auch Einblicke in das komplexe Zusammenspiel kohärenter und inkohärenter Prozesse in diesem Festkörpersystem.

Abstract

In this thesis, we experimentally study the properties of the nitrogen vacancy centre in diamond, and in particular the quantum Zeno effect (QZE) . This represents the first demonstration of the quantum Zeno effect on a single quantum system.

Due to its unique properties the nitrogen vacancy centre has become an attractive testbed for many experiments in quantum optics and viable candidate for applications in other disciplines such as magnetometry and fluorescence microscopy. We use the technique called optically detected magnetic resonance to coherently manipulate the electron spin of single nitrogen vacancy centres. This enables us to observe phenomena such as Rabi oscillations and spin echos. The final goal of our investigations is the quantum Zeno effect. The quantum Zeno effect is one of the many intriguing quantum mechanical phenomena. It describes the inhibition of coherent evolution by repeated measurements. We demonstrate this phenomenon using single nitrogen vacancy centres and gain further insights into the complex interplay between coherent and incoherent dynamics in this solid state system.

Contents

1	Introduction	1
2	Fundamentals	3
2.1	The two level system	3
2.2	The nitrogen vacancy centre in diamond	9
2.3	Photon statistics	11
3	Experimentals	15
3.1	Experimental setup	15
3.2	Methods	17
3.3	Samples	20
4	Results	21
4.1	Preliminary characterisation	21
4.2	Incoherent spin manipulation	22
4.3	Coherent manipulation of a single spin	23
4.4	Quantum Zeno effect	27
5	Conclusion & outlook	35
A	Theoretical supplement	37
	Bibliography	41

1 Introduction

Since its development in the beginning of the 20th century, quantum mechanics has proven to be a true Kuhnian revolution [1]. It was able to describe and predict a wide range of observations which had been hitherto unexplainable. Almost a hundred years later scientists still continue to discover its far reaching consequences and seek to exploit them for novel technological applications. In 1982, Richard Feynman conjectured the possibility of using intrinsic quantum properties to simulate quantum systems [2] and thereby ushered in the research in quantum information and quantum computing. Today, it has been shown theoretically that quantum computing is capable of solving certain problems (e.g. integer factorisation) more efficiently than conventional computers. At the heart of quantum computing is the quantum binary digit (qubit). In contrast to the classical bit which can only be either “0” or “1”, the qubit can be in any superposition state of the two states. So far, there have been several

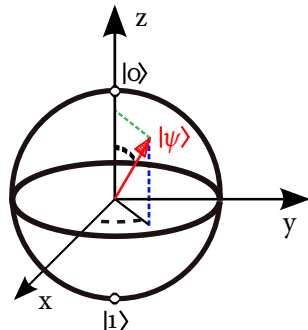


Figure 1.1: Representation of a qubit on the Bloch sphere

physical implementations of qubits such as trapped ions, electrons in quantum dots and superconducting quantum interference devices each of them having certain advantages as well as drawbacks [3]. Nitrogen vacancy (NV) centres in diamond represent an additional and very promising candidate [4, 5]. This diamond impurity exhibits some remarkable properties spurring widespread scientific research. It mirrors the behaviour of a trapped atom whilst being a genuine solid state system: a strong optical transition and an electron spin degree of freedom with a coherence time on the order of milliseconds [6].

Current state of research on NV centres

NV centres in diamond have been a very active and dynamic field of research in the past decade. From the first observation of Rabi oscillations on a single NV centre in 2004 [7] to the successful entanglement of two NV centres' spins separated by 3 meters in 2013 [8], a lot of progress has been made. This development was made possible by the increase in coherence times by two orders of magnitude from $32 \mu\text{s}$ in 2002 [9] to 2 ms in 2013 [6], manifestation of the steady progress in the fabrication techniques of artificial diamond samples. Single NV centres have also been used recently to experimentally address fundamental physical questions such as the Bell inequalities [10].

Besides their very promising use for quantum information applications, NV centres have also attracted the interest of other disciplines. In Biology, nanodiamonds have been employed as fluorescence

probes [11] and as highly sensitive thermometers in living cells [12]. They have been used as electric and magnetic field sensors [13, 14] and nanoscopic probes for mapping the local density of optical states at subwavelength scales [15].

Motivation and goal

In this work, we experimentally investigate the properties of the two level system formed by the non-degenerate spin sublevels of the NV centre's electronic ground state in diamond. In solid state systems decoherence is a major obstacle for many implementations in quantum information processing. Decoherence occurs due to incoherent interaction of the system with the environment. At first sight seemingly unrelated, the intriguing phenomenon of the quantum Zeno effect, the suppression of motion by repeated measurement, can be regarded as the limiting case of very strong decoherence.

The classical Zeno paradox was formulated in the fourth century B.C. by the Greek philosopher Zeno of Elea. He argued that if a flying arrow is observed at every instant of time it is motionless at each respective moment and hence no motion can occur in general [16]. More than 2000 thousand years later, in 1977, *Misra* and *Sudarshan* theoretically studied a quantum mechanical system under repeated observation and found what they called the quantum Zeno effect [17] paying tribute to the philosopher. They derived that, in contrast to the classical world, in the realm of quantum mechanics the coherent evolution of a quantum mechanical system can indeed be inhibited by observation. In 1990 *Itano et al.*, in the group of the Nobel prize winner *D.J. Wineland*, experimentally verified the quantum Zeno effect on an ensemble of trapped Beryllium ions.

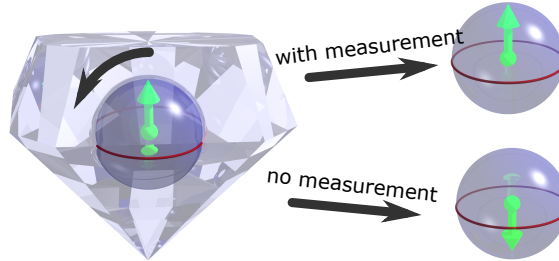


Figure 1.2: Illustration of the experiment. Initially, the electron spin of a single NV centre is prepared in the state “up”. Now, application of a microwave π -pulse flips the spin “down”. Under normal circumstances, a subsequent measurement would yield the result “down” with unity probability. However, if the spin state is measured during the microwave pulse, a second measurement performed afterwards shows an increased probability that the spin did not flip.

In this context, using single nitrogen vacancy centres in diamond, we aim to show experimentally that decoherence can deliberately be induced by means of a laser pulse destroying the phase relations (and thus inhibiting unitary evolution) in a two level system (see figure 1.2).

In the first part of this thesis we revisit some theoretical concepts relevant to the experimental studies. The experimental setup and methods are introduced in chapter 3. Equipped with these, the subsequent chapter will present some results and discuss them. Finally, a conclusion and outlook summarise and complete the work.

2 Fundamentals

This chapter introduces the theoretical principles underlying the experimental work. This comprises a very general recapitulation of two level systems as well as a brief overview of the properties of nitrogen vacancy centres. The last section covers photon statistics which is of relevance since we deal in this work exclusively with single quantum systems emitting single photons.

2.1 The two level system

2.1.1 The Bloch equations

Quantum mechanical two level systems have been extensively studied since the 1940's. They have proven not to be just of mere academic interest but have found important applications in technologies such as magnetic resonance imaging and quantum information science. The interaction between electromagnetic radiation and a two level system was first described by Bloch [18]. In our experiments, the coherent dynamics of the interaction between an applied, coherent microwave and two spin states play a central role. This can be validly described in the context of the famous Bloch equations which will be derived in the following section.

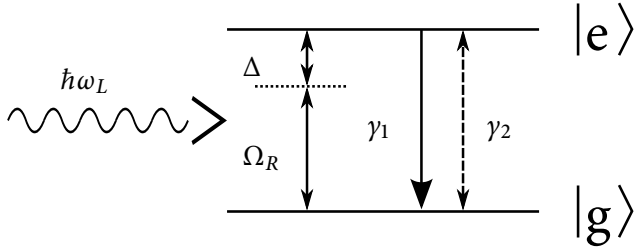


Figure 2.1: Schematic two level system with incident monochromatic light wave. Δ is the detuning, Ω_R the Rabi frequency. γ_1 and γ_2 are the longitudinal and transverse relaxation times respectively

Throughout our experiments, the electromagnetic fields interacting with the system are intense and hence it is justified to describe the fields classically while treating the two level system quantum mechanically. For the sake of simplicity we also assume the electromagnetic field to be linearly polarised parallel to the dipole axis. There are several ways for treating the problem. Since any two level system is formally equivalent to a fictitious spin- $\frac{1}{2}$, the Pauli spin matrices lend themselves to a particularly elegant solution [19, 20]. Because the set $\{\sigma_x, \sigma_y, \sigma_z, \mathbb{1}\}$ forms a complete basis for the vector space of 2×2 matrices, any 2×2 matrix can be decomposed in terms of this set. The commutation relation for the spin matrices reads

$$[\hat{\sigma}_i, \hat{\sigma}_j] = 2i \sum_{k=1}^3 \epsilon_{ijk} \hat{\sigma}_k. \quad (2.1)$$

In order to obtain the equation of motions for these operators we use the Heisenberg equation which is given by

$$i\hbar \dot{\hat{O}} = [\hat{O}, \hat{H}]. \quad (2.2)$$

for any (not explicitly time-dependent) operator \hat{O} . The Hamiltonian of the entire system is constituted by two terms:

$$\hat{H} = \hat{H}_{at} + \hat{H}_{int}. \quad (2.3)$$

\hat{H}_{at} is the atomic Hamiltonian describing the unperturbed two level system and \hat{H}_{int} , the interaction Hamiltonian, stands for the coupling of the two level system to the electromagnetic field. The atomic Hamiltonian written in our basis set reads

$$\hat{H}_{at} = \frac{1}{2}(W_+ + W_-)\mathbb{1} + \frac{1}{2}(W_+ - W_-)\hat{\sigma}_z, \quad (2.4)$$

where W_+ and W_- represent the energies of the upper or lower eigenstate respectively. The interaction Hamiltonian for a monochromatic, linearly polarised incident field $\mathcal{E}(t) = \mathcal{E}_0 \cos(\omega_L t)$ reads in the dipole approximation

$$\hat{H}_{int} = d_{12}\mathcal{E}_0 \cos(\omega_L t)\hat{\sigma}_x, \quad (2.5)$$

where d_{12} is the electric dipole moment between the states 1 and 2 and \mathcal{E}_0 the amplitude of the electric field. Since the first part in eq. 2.4 is proportional to the identity matrix it commutes with any matrix and thus does not contribute in the equations of motion. It is sufficient to use

$$\hat{H} = \frac{1}{2}(W_+ - W_-)\hat{\sigma}_z - d_{12}\mathcal{E}_0 \cos(\omega_L t)\hat{\sigma}_x, \quad (2.6)$$

Plugging this into eq. 2.2 and taking the expectation value gives the Bloch equations

$$\frac{d}{dt}\langle\hat{\sigma}_x\rangle = -\omega_0\langle\hat{\sigma}_y\rangle, \quad (2.7a)$$

$$\frac{d}{dt}\langle\hat{\sigma}_y\rangle = \omega_0\langle\hat{\sigma}_x\rangle + \Omega_R\langle\hat{\sigma}_z\rangle(e^{i\omega_L t} + e^{-i\omega_L t}), \quad (2.7b)$$

$$\frac{d}{dt}\langle\hat{\sigma}_z\rangle = -\Omega_R\langle\hat{\sigma}_y\rangle(e^{i\omega_L t} + e^{-i\omega_L t}), \quad (2.7c)$$

where we have introduced the Rabi frequency $\Omega_R = \frac{d_{12}\mathcal{E}_0}{\hbar}$ and the transition frequency of the atomic levels $\omega_0 = \frac{W_+ - W_-}{\hbar}$ and the chevrons $\langle\dots\rangle$ denote the average value. Identifying the mean values of the spin operators with the components of a vector $\mathbf{r} = (\langle\hat{\sigma}_x\rangle, \langle\hat{\sigma}_y\rangle, \langle\hat{\sigma}_z\rangle)$ we obtain the well known Bloch vector depicted in figure 2.2.

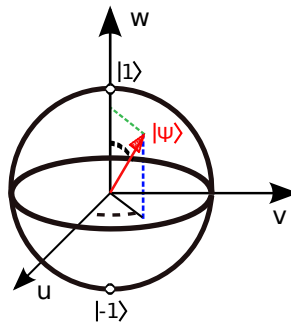


Figure 2.2: The Bloch vector of a pure state on the Bloch sphere.

The isomorphy of this problem to a spin in an effective magnetic field $B = B_0 + B(t)$ can be made apparent by considering the Hamiltonian $H = -\mathbf{M}\mathbf{B}(t) = -\gamma\mathbf{S}(\mathbf{B}_0 + \mathbf{B}_1(t))$. Here, $\mathbf{B}_0 = (0, 0, B_0)$ is a static magnetic field in z direction and $\mathbf{B}(t) = (B_x \cos(\omega t), 0, 0)$ is a time dependent wave, polarised in the x direction while γ denotes the gyromagnetic ratio. Thus we obtain

$$H = -\mathbf{M}\mathbf{S} = -\frac{\gamma\hbar}{2}B_0\hat{\sigma}_z - \frac{\hbar}{2}B_x \cos(\omega t)\hat{\sigma}_x, \quad (2.8)$$

which is formally identical to eq. 2.6. From the first term in eq. 2.8 it is also evident that the splitting between the two states depends linearly on the field strength of the applied static field B_0 .

Rotating wave approximation

The eq. 2.7 is formally equivalent to the classical problem of a spinning top whose evolution is governed by the equation

$$\dot{\boldsymbol{\rho}} = \boldsymbol{\Omega} \times \boldsymbol{\rho} \quad (2.9)$$

if the “torque” vector has the components $\boldsymbol{\Omega} = (-2\Omega_R \cos(\omega t), 0, \omega_0)$. However, in contrast to the spinning top exposed to a static gravitational field, the magnetic field considered here is time dependent which leads to extremely complicated dynamics. The problem is considerably simplified by application of the rotating wave approximation (RWA) which effectively renders the coefficients in eq. 2.7 time independent. First, we transform the vector \mathbf{r} into a frame rotating at the constant frequency ω_L ($\mathbf{r} = (\langle \hat{\sigma}_x \rangle, \langle \hat{\sigma}_y \rangle, \langle \hat{\sigma}_z \rangle) \rightarrow \boldsymbol{\rho} = (u, v, w)$). This is achieved by the following rotation matrix describing a rotation about the z-axis:

$$\boldsymbol{\rho} = \begin{pmatrix} \cos(\omega_L t) & \sin(\omega_L t) & 0 \\ -\sin(\omega_L t) & \cos(\omega_L t) & 0 \\ 0 & 0 & 1 \end{pmatrix} \mathbf{r}. \quad (2.10)$$

The dynamics of the vector \mathbf{r} observed in the rotating frame are obtained accordingly by transformation of eq. 2.7, which yields

$$\dot{\boldsymbol{\rho}} = \begin{pmatrix} 0 & -(\omega_0 - \omega_L) & -\Omega_R \sin(2\omega_L t) \\ (\omega_0 - \omega_L) & 0 & \Omega_R(1 + \cos(2\omega_L t)) \\ \Omega_R \sin(2\omega_L t) & -\Omega_R(1 + \cos(2\omega_L t)) & 0 \end{pmatrix} \boldsymbol{\rho}. \quad (2.11)$$

Secondly, if we now neglect the terms counter-rotating at twice the frequency of the field we obtain the following set of coupled differential equations where $\Delta = \omega_0 - \omega_L$ denotes the detuning between the light wave and the transition frequency:

$$\frac{d}{dt}u = -\Delta v, \quad (2.12a)$$

$$\frac{d}{dt}v = \Delta u + \Omega_R w, \quad (2.12b)$$

$$\frac{d}{dt}w = -\Omega_R v. \quad (2.12c)$$

The aforementioned rotating wave approximation is an often applied and valid assumption in atomic

2 Fundamentals

physics as long as $|\omega_0 - \omega_L| \ll \omega_0$ [21, 22]. The physical meaning of the different components u, v and w can be recovered by considering the Hamiltonian. w , the trace over $\hat{\sigma}_z$, represents the population difference (often called inversion). u and v are proportional to the components of the averaged electric dipole moment of the system $\langle \hat{d} \rangle = d_{12} \text{Tr}\{\hat{\rho}\hat{\sigma}_x\} = d_{12}(u \cos(\omega_L t) - v \sin(\omega_L t))$.

Rabi oscillations

The foregoing derivation exploited the findings by Feynman et al. [23] that any two level system can be geometrically represented by the 3 dimensional ‘‘Bloch vector’’ $\rho = (u, v, w)$ obeying equation 2.12. In an isolated system the vector’s motion is confined to the surface of the Bloch sphere. A well known set of analytical solutions for the equations 2.12 describing oscillations of the atomic inversion were found by Rabi in 1937 [24]

$$w(t; \Delta) = -u_0 \frac{\Delta \Omega_R}{\Omega^2} (1 - \cos(\Omega t)) - v_0 \frac{\Omega_R}{\Omega} \sin(\Omega t) + w_0 \frac{\Delta^2 + \Omega_R^2 \cos(\Omega t)}{\Omega^2}, \quad (2.13)$$

where $\Omega = \sqrt{\Delta^2 + \Omega_R^2}$ designates the generalised Rabi frequency. Rabi oscillations for a system initially prepared in the lower state ($w(0) = -1, u(0) = v(0) = 0$) are shown for different values of the detuning Δ in figure 2.3. A detuning of $\Delta \neq 0$ reduces the contrast, while increasing the frequency at the same time. Experimentally observed for the first time in 1949 [25], they have been observed on a wide array of systems since then, including the electronic spin of a single NV centre in 2004 [7].

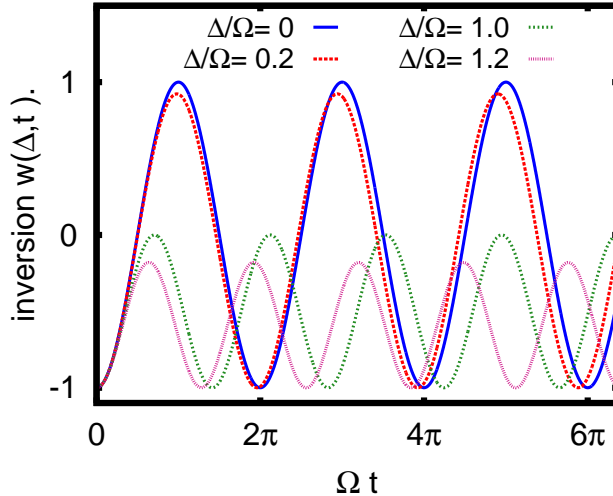


Figure 2.3: Rabi oscillations for a system initially prepared in $w(0) = -1$. The blue and red curves are for $\frac{\Delta}{\Omega} = 0$ and for $\frac{\Delta}{\Omega} = 0.2$, respectively. The green and violet curve represent the Rabi oscillations for $\frac{\Delta}{\Omega} = 1$ and $\frac{\Delta}{\Omega} = 1.2$.

2.1.2 Effects of decoherence

Interactions of a quantum system with its environment inevitably entail the loss of coherence between the quantum states of the system. This decoherence can arise for a number of different reasons depending on the specific system. One characteristic consequence of decoherence is for example the suppression of interference [26].

The Bloch equations derived in the previous section can be extended to take these relaxation processes into account. To this end, it is customary to extend the Bloch equations by phenomenological damping terms first introduced by Bloch for nuclear magnetic resonance (NMR). The decay constant of the inversion is usually labeled T_1 , whilst T_2 is assigned to the decay time of the coherences.

In NMR, one further distinguishes between decoherence due to homogeneous interactions labeled by T'_2 and inhomogeneous contributions to the decoherence are usually denoted by T_2 . Hence the total coherence decay time is given by:

$$\frac{1}{T_2^*} = \frac{1}{T'_2} + \frac{1}{T_2}. \quad (2.14)$$

Furthermore, the decay time T_1 sets an upper bound to the maximally achievable decoherence time given by the relation

$$\frac{1}{2T_1} \leq \frac{1}{T_2^*}. \quad (2.15)$$

In order to account for an equilibrium value of the inversion unequal to -1, the constant w_{eq} can be introduced. Accordingly, the equations of motion of the components of the Bloch vector $\rho = (u, v, w)$ in the rotating frame can be rewritten as

$$\frac{d}{dt}u = -\Delta v - \frac{u}{T_2^*}, \quad (2.16a)$$

$$\frac{d}{dt}v = \Delta u + \Omega_R w - \frac{v}{T_2^*}, \quad (2.16b)$$

$$\frac{d}{dt}w = -\frac{w - w_{eq}}{T_1} - \Omega_R v. \quad (2.16c)$$

The loss of coherence leads to an exponential dampening of the observable Rabi oscillations which, in the case of resonant excitation, can be described by the following:

$$w(t) = w_0 e^{-\frac{t}{2T_2^*}} \cos(\Omega_R t). \quad (2.17)$$

The introduced decay constants have been initially developed for the description of the evolution of an ensemble of spins. For single quantum systems however, as in our case, the terminology can be adopted. It has become convention to designate low frequency noise that can be removed via an experimental technique called “echo sequences” as T'_2 [27].

2.1.3 Quantum Zeno effect

In 1977, Misra and Sudarshan proved that the evolution of a quantum mechanical system can be brought to an halt by repeated observation [17]. We take a somewhat less sophisticated approach [26] and consider again a two level system where the system is initially prepared in state $|u\rangle$. Unitary evolution leads to a superposition of this intial state and the orthogonal state $|d\rangle$:

$$|\psi(t)\rangle = \hat{U}|u\rangle = a_u(t)|u\rangle + a_d(t)|d\rangle. \quad (2.18)$$

2 Fundamentals

where $\hat{U} = e^{-i\hat{H}t}$ is the time evolution operator for time-independent Hamiltonians ($\hbar = 1$). Expanding

$$\hat{U} = \mathbb{1} - i\hat{H}t - \frac{1}{2}\hat{H}^2t^2 + \dots \quad (2.19)$$

and calculating the probability $P(\tau)$ that at some later instant τ the system is still found in its undecayed state $|u\rangle$ yields

$$\begin{aligned} P(\tau) &= |a_u(\tau)|^2 = |\langle u| \hat{U} |u\rangle|^2 \\ &\approx 1 - (\Delta\hat{H})^2\tau^2 + O(\tau^4), \end{aligned} \quad (2.20)$$

where $(\Delta\hat{H})^2 = \langle u| \hat{H}^2 |u\rangle - \langle u| \hat{H} |u\rangle^2$.

If, instead of being performed once, the measurement is repeated N times during the interval $[0, t]$ the probability of finding the system still in the initial state is given by

$$P_N(t) \approx [1 - (\Delta\hat{H})^2(\frac{t}{N})^2]^N \geq 1 - (\Delta\hat{H})^2\tau^2 = P(t). \quad (2.21)$$

Hence the transition probability is always suppressed. Taking the limit of arbitrarily dense measurements, the transition can be stopped altogether

$$P_N(t) \approx 1 - ((\langle u| \hat{H}^2 |u\rangle - \langle u| \hat{H} |u\rangle^2)(\frac{t}{N})^2 + \dots) \xrightarrow{N \rightarrow \infty} 1. \quad (2.22)$$

The quadratic time dependence term of transition probabilities is important in the short-time limit as is apparent from the preceding derivation. Hence it can in particular be observed in induced coherent transitions following a sinusoidal evolution as opposed to an incoherently, exponentially decaying state where indeed the phenomenon is expected to be not observable [26].

The quantum Zeno effect is a phenomenon touching the very core of quantum mechanics and its interpretations, in particular the concept of a measurement. At its inception, von Neumann formulated the “collapse” postulate which states that a measurement always finds a quantum mechanical system in one of the eigenstates of the corresponding basis but never in a superposition state. Hence the wavefunction is said to collapse. A more modern view could be to regard a measurement as an extremely strong decoherence [28]. To this day, the different interpretations of quantum mechanics yielding identical, experimentally verifiable predictions appear to be a matter of personal preference [29–31].

2.2 The nitrogen vacancy centre in diamond

After having presented some concepts fundamental to the studies of two-level systems in the preceding chapter, we now introduce the specific object of the experimental investigation, the nitrogen vacancy centre in diamond.

Diamond is a wide band gap semiconductor with a band gap of 5.5 eV and a refractive index of 2.4. It is the hardest known bulk material and boasts the highest thermal conductivity of any material. Its wide band gap render diamond transparent for electromagnetic radiation from the ultraviolet to the infrared. There are more than 500 known luminescent defect centres in diamond [32].

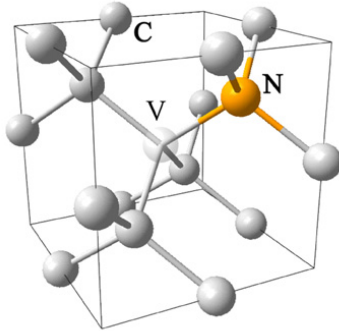


Figure 2.4: A crystallographic model of the nitrogen vacancy centre in diamond. Taken from [33].

Among them, the nitrogen vacancy (NV) is certainly the most prominent one. It consists of a substitutional nitrogen atom adjacent to a vacancy in the diamond host lattice (cf. figure 2.4). There are two optically active variants of the NV centre, the neutral NV^0 and the negatively charged NV^- . In this work, we will exclusively treat the NV^- and will henceforth simply refer to it as NV. Experimental investigations have established that the NV centre is an effective spin 1 system with a triplet ground state. Three dangling bond electrons provided by carbon atoms, two nitrogen electrons and one extra electron constitute its 6 electrons. The level scheme depicted in figure 2.6 is given by its c_{3v} symmetry although there is still an ongoing debate about the exact nature of the metastable singlet state [34].

2.2.1 Optical properties

A characteristic optical feature of the NV centre is the zero phonon line (ZPL) at 637 nm (see figure 2.5) with a Fourier-limited intrinsic line width of around 10 MHz [35]. This is however only observable in bulk samples under resonant excitation at cryogenic temperatures. Otherwise, the ZPL suffers from spectral diffusion [36], limiting the NV centre's applicability in areas where a high degree of photon-indistinguishability is desired [37].

Radiative transitions couple strongly to the phonon side band of the ground state leading to a wide emission band extending up to 800 nm as is evidenced in figure 2.5.

The phonon side band accounts for roughly 95 % of the emission even at cryogenic temperatures. The fluorescence lifetime of the excited state in a bulk sample is around 10 ns [38]. This wide emission band poses certain problems to the NVs suitability for implementations in photonic quantum technology, e.g. the coupling of the emission to cavities [39, 40]. The excited state phonon side band also allows to optically excite the system off-resonantly which is, conveniently, possible at a wavelength of 532 nm. Furthermore, the NV centre is a photo-stable emitter of single photons even at room temperature (see section 2.3) [38]. Typical emission rates are on the order of $40 \cdot 10^3$ and $200 \cdot 10^3$ counts s^{-1} for

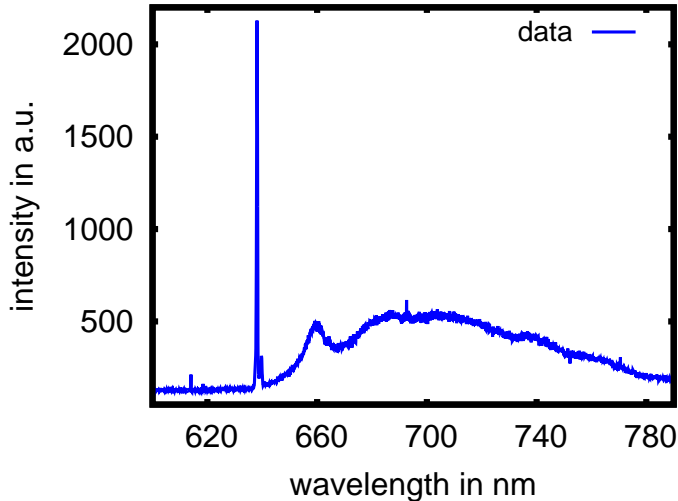


Figure 2.5: Fluorescence emission spectra of a single NV in a bulk sample at 5.1 K. The sharp peak at 637 nm is the ZPL. The phonon side band stretches from 650 nm to around 780 nm.

bulk and nanodiamond samples respectively (at reported detection efficiencies between 1 and 2%) [33]. Non-radiative transitions via the shelving state lead to a quantum yield of around 0.7 [41].

2.2.2 Spin properties

Apart from its optical properties, it is in particular its remarkable spin properties that attract most of the research on NV centres. The electronic level structure at room temperature is displayed in figure 2.6 alongside the excited state structure at cryogenic temperatures. As mentioned above, the electronic ground state is a triplet state. Its zero field splitting caused by the crystal field is 2.87 GHz [42], which is also weakly dependent on temperature and crystal strain [43]. Interestingly, excitation spectra of the optical ZPL at low temperatures revealed a very complex fine structure in the excited state. This turned out to be due to spin-orbit, spin-spin interaction and especially transverse strain perpendicular to the NV centre's axis [44]. In fact, the 3E excited state is split into two branches, each consisting of three states. Whilst in the upper branch E_x the spin sublevels show no sign of crossing, at high strain spin mixing occurs in the lower branch E_y , leading to fully allowed spin-flip optical transitions if the lower branch is excited [45]. The observed room temperature level splitting can thus be attributed to an averaging over both branches [46]. Spin selective optical transitions between the ground and excited state can be resonantly driven at cryogenic temperatures which is a prerequisite for high fidelity spin-spin or spin-photon entanglement [8, 47]. While optical transition to the excited state is spin preserving to a high degree [48], the decay from the lower branch occurs with equal probabilities to the $m_s = 1$ and $m_s = -1$ state. Thus, spin-flip transitions are possible due to high strain in the lower branch. Moreover, the transitions to the metastable singlet state 1A is highly spin state dependent enabling the optical read-out of the spin state (cf. section 3.2).

2.2.3 Classification of diamond

There are different classifications of diamond depending on the concentration of nitrogen which are labeled type I and type II with the latter being relatively free of nitrogen [49]. The classes can be further subdivided in Ia, Ib and IIa and IIb respectively. Most natural diamonds belong to the Ia type where

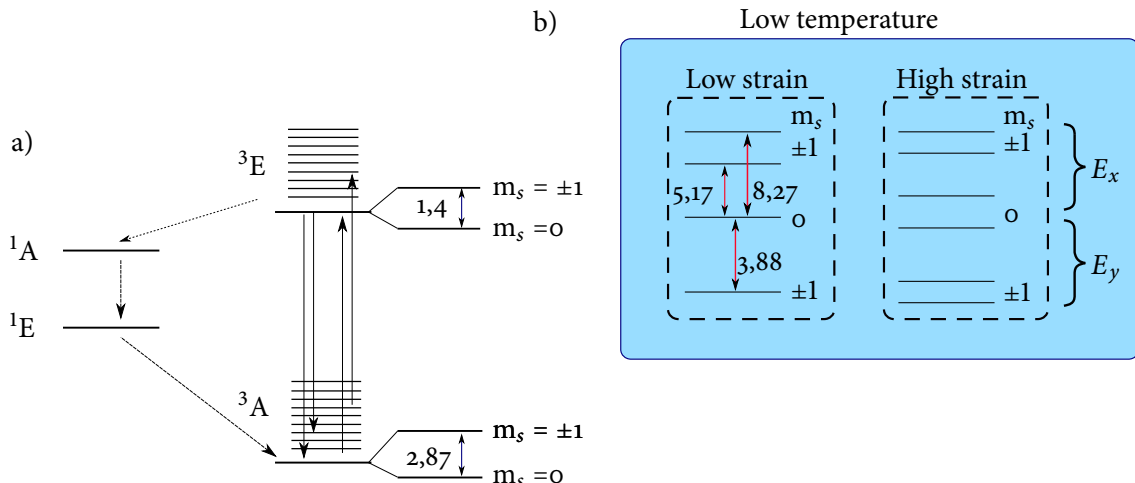


Figure 2.6: a) Level scheme of the NV centre in diamond at roomtemperature. b) level splitting of the excited state at cryogenic temperatures with low and with high strain respectively. The indicated level splittings are given in GHz.

nitrogen is present in aggregated form reaching concentrations as high as 3000 ppm. In type Ib diamond nitrogen exists as single substitutional atom with typical concentrations of 40 ppm. Since less than 0.1% of naturally occurring diamond are Ib diamonds, most diamonds used in R&D are artificially synthesised using either the high-pressure high-temperature (HPHT) technique or chemical vapour deposition (CVD). Reflecting the natural abundance of the two stable isotopes of carbon, diamond is formed of 98.9% ¹²C and 1.1 % ¹³C unless isotopically engineered. Since decoherence is a major issue in the field of quantum optics with NV centres it is preferable to work with samples with low concentration of ¹³C ($I = \frac{1}{2}$) as it is their nuclear spin that mainly causes the decoherence of the NV centre's electron spin [50].

For different purposes two kinds of samples are generally used in scientific research: diamond bulk samples and nanodiamonds (NDs) which are tiny crystals with sizes ranging typically from 10-100nm. Due to their size being considerably smaller than the emitted wavelength, NDs can be considered as point-like emitters offering very high photon emission rates compared to bulk samples whose emission rate is reduced due to refraction at the diamond-surface interface. With regard to the spin properties, bulk samples exhibit in general considerably longer spin coherence times. Furthermore, the spectral diffusion of the ZPL is significantly slower than in NDs. Thus bulk samples are preferred in quantum information implementations [51] whereas NDs are utilised for photonic hybrid devices [52] and biological applications [53, 54].

2.3 Photon statistics

Using the Coulomb gauge and quantising the electromagnetic field contained in a cubic empty box with periodic boundary conditions leads to the following expression for the electric field

$$\hat{E}(\mathbf{r}) = \sum_j i \sqrt{\frac{\hbar \omega_j}{2\epsilon_0 L^3}} [\hat{a}_j \mathbf{e}_j e^{i(k_j r - \omega_j t)} + \hat{a}_j^\dagger \mathbf{e}_j e^{-i(k_j r - \omega_j t)}] = \hat{E}^{(+)} + \hat{E}^{(-)}, \quad (2.23)$$

where L is the length of the box, \mathbf{e}_j the polarisation vector and \hat{a}_j^\dagger and \hat{a}_j the usual bosonic creation and annihilation operator of the j th mode, respectively.

Correlation functions are an important tool for proving the quantum nature of the electromagnetic field. In quantum optics, correlation functions are used to obtain information about the coherence properties of the electromagnetic field [55]. The correlation function of the n^{th} -order can be defined as

$$G^{(n)}(x_1..x_n, x_{n+1}..x_{2n}) = \text{Tr} \left\{ \rho \hat{E}^{(-)}(x_1) .. \hat{E}^{(-)}(x_n) \hat{E}^{(+)}(x_{n+1}) .. \hat{E}^{(+)}(x_{2n}) \right\}, \quad (2.24)$$

where $x_n = (t_i, \mathbf{r}_i)$ are different space-time points. The two point correlation function measures the joint photon count probability of detecting a photon at time t and another one at $t + \tau$. The expression

$$g^{(2)}(\tau) = \frac{G^{(2)}(\tau)}{|G^{(1)}(0)|^2} \quad (2.25)$$

defines the normalised second order correlation function. The correlation function $g^{(2)}(0)$ allows to determine whether the light source is bunched, Poissonian or anti-bunched:

Bunched: $g^{(2)}(0) > 1$ The conditional probability of simultaneously detecting two photons is increased. Light typically emitted from thermal light sources.

Poisson-like: $g^{(2)}(0) = 1$ The emitted light follows a Poisson distribution. Light emitted by an ideal laser.

Anti-bunched: $g^{(2)}(0) < 1$ The conditional probability of simultaneously detecting two photons is decreased. Light emitted by a single quantum object

Assuming a monochromatic excitation of the electromagnetic field with n photons equation 2.25 at time $\tau = 0$ yields:

$$g^{(2)}(0) = \frac{\langle \hat{a}^\dagger \hat{a}^\dagger \hat{a} \hat{a} \rangle}{\langle \hat{a}^\dagger \hat{a} \rangle^2} = 1 - \frac{1}{n}. \quad (2.26)$$

Thus, an experimentally recorded value of $g^{(2)}(0) \leq \frac{1}{2}$ is a strong indication that the observed light stems predominantly from one single photon emitter only. The plots obtained from evaluating eq. 2.25, assuming non-classical, coherent and thermal light are shown in figure 2.7a. Experimentally detected $G^{(2)}$ functions of course deviate from the theory for a number of reasons, most notably due to the level structure of the emitter, background fluorescence of the sample and noise. Therefore one can make several approximations enabling a quantitative analysis of the $g^{(2)}$ function. For the NV centre, simplified as a three-level system (cf. figure 2.7b) described by a rate equation, one can derive the following formula [38]:

$$g^{(2)}(\tau) = 1 + (1 - C)e^{\Gamma_1 \tau} + Ce^{\Gamma_2 \tau}. \quad (2.27)$$

The decay times $\Gamma_{1/2}$ and coefficient C are given by:

$$\Gamma_{1/2} = \frac{-A \pm \sqrt{A^2 - 4B}}{2}, \quad (2.28a)$$

$$C = \frac{\Gamma_2 + k_{31} - k_{12} \frac{k_{23}}{k_{31}}}{\Gamma_1 - \Gamma_2}, \quad (2.28b)$$

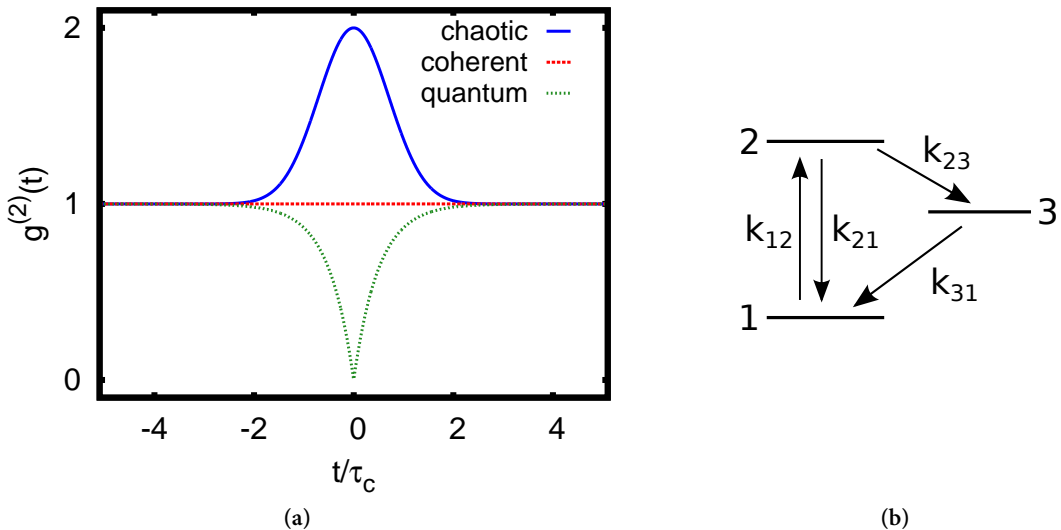


Figure 2.7: (a) $g^{(2)}(t)$ for different light sources. The blue curve is a chaotic light source. The red curve is characteristic for coherent light source while the dashed green curve is light emitted by a single two-level emitter. (b) 3 level system used for deriving $g^{(2)}(\tau)$ of the NV centre.

where

$$A = k_{12} + k_{21} + k_{23} + k_{31}, \quad (2.29a)$$

$$B = k_{31}(k_{21} + k_{12}) + k_{23}(k_{31} + k_{12}). \quad (2.29b)$$

The experimental detection of the two point correlation function is described in section 3.2.

3 Experimentals

After the presentation of the theoretical fundamentals in the preceding chapter, we describe the experimental setup and individual devices utilised during the experiments in the first section of this chapter. The second section explains the applied techniques and methods while the last section describes the samples and their preparation.

3.1 Experimental setup

The experimental setup utilised for studying the NV centres is schematically drawn in figure 3.1. It is essentially a home build confocal scanning microscope incorporating microwave (MW) coupling and a Hanbury Brown and Twiss interferometer.

Two lasers were used to excite the sample off-resonantly: a fibre-coupled continuous-wave (cw) and a pulsed diode laser both emitting at 532 nm. The beam of the cw laser was switched using an acusto-optical modulator (AOM). The sample was scanned in the x-y plane using piezo controlled mirrors and a piezo mount by *PiezoJena* for the z-axis which is not shown for simplicity. The sample could be mounted either inside a cryostat for studies at cryogenic temperatures down to 4.7 K or on a 3d manual stage for experiments at room temperature. The lasers were focused through a high NA objective lens (NA=0.9, working distance 0,7 mm). The fluorescence is collected through the same lens and separated from the laser light using a dichroic mirror and two long pass filters. Ultimately, two avalanche photo diodes detected the fluorescence signal. The signal was processed with a *National Instrument* data acquisition card (*NI PCI-6014*) allowing for time-gated detection. The different devices used for the experiment were synchronised using the *USB-BITP-200* bit pattern generator from *Deditec*. For samples with a structured surface a LED served as light source and a charge-coupled device (CCD) camera was used for orientation. The main components of the setup are detailed below.

Cryostat

In order to perform low temperature studies, the samples were placed inside a *CryoVac Microcryo* cryostat. This cryostat is a continuous flow liquid-helium cryostat whose specific design with the objective lens being inside the isolation vacuum chamber enables the use of high NA objectives as well as avoiding losses and focus distortion due to scattering at an additional interface. The lowest attainable temperature is 4.7 K. The vacuum chamber was evacuated using a *Pfeiffer Vacuum* pump consisting of a rotative pump coupled to a turbo-molecular pump with a ionisation gauge device incorporated for monitoring the pressure. The maximally achievable pressures are on the order of 10^{-7} mbar.

Laser sources

During our experiments we used a frequency doubled cw diode laser (*Shanghai Laser & Optics Century Co. GL532T3-200*) with an emission at 532 nm for off-resonant excitation of our samples. The maximally attainable output power was 500 mW. The maximal excitation power measured before the objective was 2 mW which was sufficient to saturate the optical transition of a NV centre. It was switched on

3 Experiments

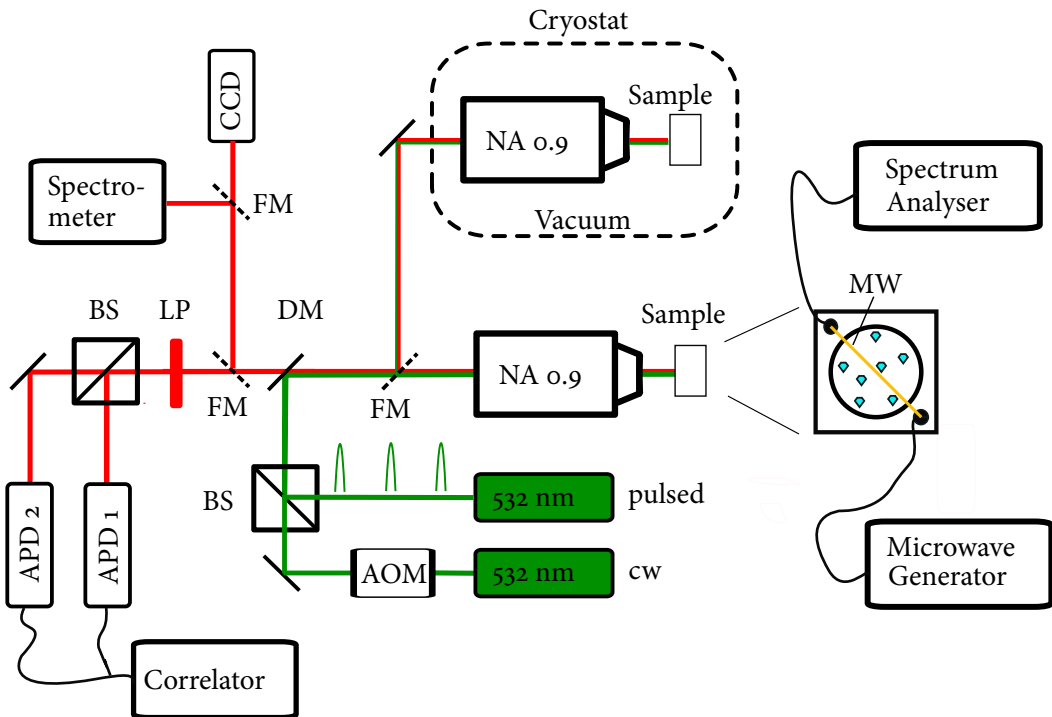


Figure 3.1: Experimental setup used for performing experiments. Abbreviations: BS-beamsplitter, LP-longpass filter, DM- dichroic mirror, FM- flippable mirror, APD- avalanche photo diode, AOM-acousto-optical modulator. See main text for details.

and off using an *MT110-A1-VIs* AOM from *AA opto-electronic* with an extinction ratio of 2000:1 and a switching time of around 18 ns.

Alternatively a pulsed frequency doubled diode laser (*PicoQuant LDH-P-FA-530XL*) had been coaligned with the cw laser for pulsed excitation of the NV centres. Its pulse width (FWHM) is below 100 ps with a freely adjustable repetition rate between 1 and 80 MHz. The average output power at a repetition rate of 80 MHz is more than 200 mW. The laser was controlled using the *PicoQuant PDL 800-D pulsed laser driver* which allows the laser pulses to be triggered by an external device. Both devices were kindly provided by *PicoQuant*.

Photon detection

The photons were detected using two single photon counting silicon avalanche photo diodes (APD) from *Laser Components*. The dark count rate of each module is below 20 cts/s and their quantum efficiency is around 73 %. The two point correlation functions were obtained via a Hanbury Brown-Twiss interferometer by connecting both modules to a *PicoQuant TimeHarp 200* which measures the time delay between detection events on the two APDs. The *TimeHarp* allows measuring intensities of up to 3 million cts/s with a temporal resolution of less than 40 ps. Fluorescence lifetime measurements where recorded using the *TimeHarp* by triggering it externally either from a laser source or the bit pattern generator.

Spectrometer

We used a 500 mm spectrograph unit (*Acton SpectraPro 500i*) in order to record emission spectra of the studied NV centres. The unit includes a liquid-nitrogen cooled charge-coupled device (CCD) chip.

An automatically controllable turret with three different gratings (600, 1200 and 1800 grooves/inch) provided different spectral resolutions (FWHM: 0.085 nm and 0.038 nm and 0.027 nm respectively at a wavelength of 637 nm) within the chosen wavelength range.

CCD camera

The CCD camera used for adjustment and orientation on the bulk sample is a *Hamamatsu Digital Camera ORCA-HR C4742-95*. Its peltier cooled chip has 10 million pixels with the shortest possible exposure time being 330 μ s.

Microwave generation

For the generation of the microwave radiation we used a serially (RS232) addressed *Hameg HM8135 Synthesizer* capable of generating cw signals in the frequency range from 1Hz to 3 GHz with a maximum power of 13 dBm. The microwave pulses were generated using ZASW-2-50DR+ switches from *Mini-Circuits*. They have typical switching times of 10 ns. Afterwards, the microwave was passed through a MW-amplifier to attain powers of up to 35 dBm which corresponds to roughly 3,2 Watt. After passing the experimental setup the generated microwaves could be spectrally analysed using a spectrum analyser.

Bit pattern generator

A *USB-Bit Pattern Generator-200* from *Deditec* was used to synchronise and trigger the various devices used in the experiments. It allows to simultaneously generate digital patterns on 36 output channels with a maximum sampling rate of 150 MHz. One bit pattern is 36 bits wide while the internal RAM allows to store 512k bit patterns per channel.

3.2 Methods

The following section contains a brief description of the concepts underlying confocal microscopy, the Hanbury Brown and Twiss (HBT) interferometer, and optically detected magnetic resonance (ODMR) as well as their specific implementation in our setup.

Confocal microscopy

Confocal microscopy offers an enhanced resolution especially in the axial direction and improved signal to noise ratio compared to conventional wide field microscopes [56]. A sketch is depicted in figure 3.2a. The fundamental differences compared to wide field microscopy are that a focused light beam is used to excite the sample and the use of an aperture in the focal plane to spatially filter the image and select the focal spot. In our setup, we use the same object lens for excitation and collecting the signal. A dichroic mirror and additional long pass filters are used to separate the excitation beam from the collected fluorescence. In order to scan the samples we use two mirrors mounted on piezo elements which allow to displace the beam laterally with a resolution of less than 10 nm.

Hanbury Brown and Twiss Interferometer

As stated in section 2.3 the second order autocorrelation function $g^{(2)}(\tau)$ is employed to determine the coherence properties of the detected light. This necessitates the recording of time delays between photon pairs on a time scale less than the emitter's life time. However, a problem is posed by the dead

3 Experimentals

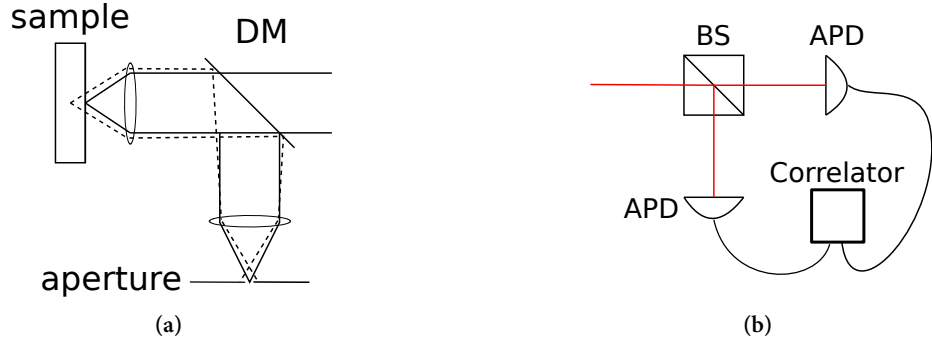


Figure 3.2: (a) Sketch of a confocal microscope. (b) Sketch of a HBT interferometer.

time of the detectors which often exceeds the life time of the emitter. This obstacle is overcome by using a HBT setup. A HBT interferometer consists of a 50/50 beam splitter and two avalanche photo diodes placed at either end of the interferometer arm. The time difference between two subsequent photons is thus determined by using a start trigger (event on APD 1) and a stop signal (event on APD 2). A time delay of around 220 ns between the two arms is introduced by using differently long cables (cf. figure 3.2b). This allows to directly record the $g^{(2)}\tau$ function also for negative τ .

Optically detected magnetic resonance

Due to the small magnetic moment, electron or nuclear spin resonance experiments usually require to be ensembles of typically 10^{12} spins [57]. Furthermore, at room temperature the population inversion between the two spin states is almost zero in equilibrium. However, it is possible to enhance the sensitivity by detecting the magnetic resonance effect in the optical regime which is referred to as optically detected magnetic resonance. This technique in combination with confocal microscopy lead to the first detection of a single spin in 1993 [58]. Because of the level structure of the NV centre, this technique can also be applied for detecting the NV centre's spin state. The principle is most easily understood by considering the NV centre's simplified level scheme shown in figure 3.3a. Upon optical

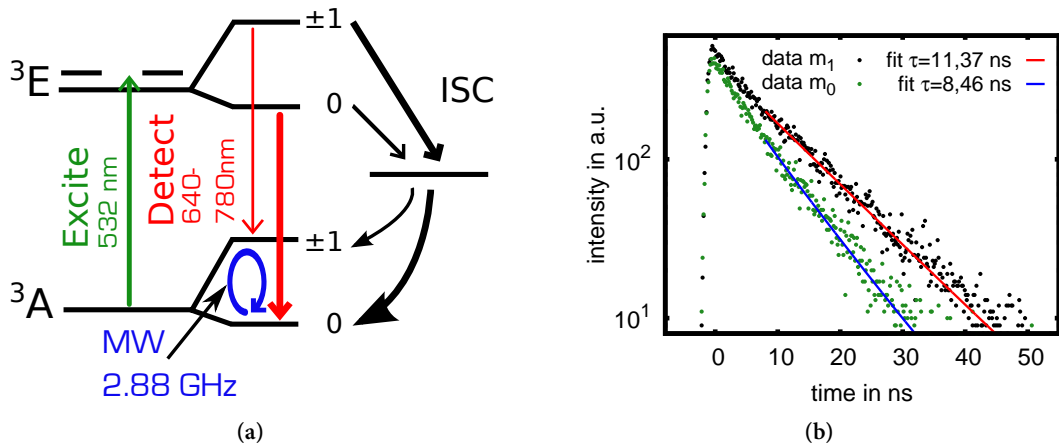


Figure 3.3: (a) Simplified level scheme of NV centre with relevant transitions. (b) Fluorescence decay of a NV centre initially prepared in the $m_s = 0$ and $m_s = 1$ state in a bulk sample, respectively.

excitation which is mainly spin conserving [48] the NV centre can relax either radiatively from 3E to 3A or non radiatively via intersystem crossing (ISC) . The ISC rate to the singlet manifold is however highly spin state dependent being on the order of three magnitudes higher for spin $m_s = \pm 1$ states compared to the spin $m_s = 0$ state [4] which corresponds to a shorter fluorescence life time as is illustrated by figure 3.3b. Relaxation from the intermediate singlet state (deshelving) predominantly populates the $m_s = 0$ of the ground state. Thus, by optically pumping the NV centre off-resonantly for a few microseconds one can initialise the NV centre in the $m_s = 0$ state with reported polarisation ranging from 42-96% [59]. Because the deshelving rate is lower than the fluorescence rate, the spin $m_s = 0$ state appears brighter than the spin $m_s = \pm 1$ state [60].

Throughout our experiments we use different microwave pulse sequences to coherently manipulate the electronic spin of the NV centre. However, the protocol employed for optical read-out and initialisation which is shown in figure 3.4 is used in all of them. As discussed above, the laser serves for both, initialisation and read-out of the spin state. The NV centre is first polarised by irradiation with the green laser at 532 nm for about 3 μs . During the last 500 ns of the laser pulse photons are counted for normalisation reference to compensate for eventual fluctuations in the emitted intensity during one experiment. The laser is then turned off and the respective microwave pulse sequence is executed. Finally, the green laser is switched on again for optical read-out. The emitted fluorescence, shown in figure 3.4, is recorded by an independent second counter during the first 300 ns. As can be seen, the fluorescence signals are spin state dependent with the shaded area indicating the contrast used for distinguishing the two spin states. Using this technique optical initialisation and read-out of the NV centre's spin is possible. It allows to determine the average spin state of the NV centre within a few thousand optical cycles.

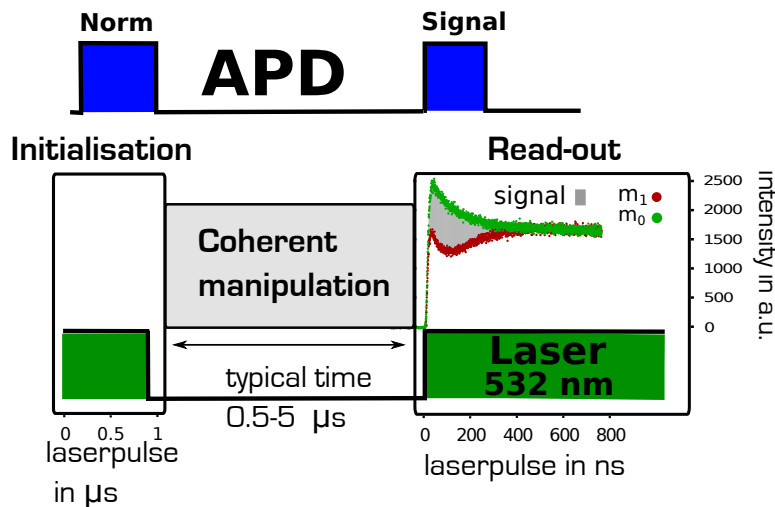


Figure 3.4: Scheme of the general measurement protocol. The exact length of the coherent manipulation depends on the specific experiment. Read-out frame: The grey area between the two fluorescence curves is the signal used to distinguish the two spin states.

Despite the incredible success in the application of this technique to NV centres, deeper understanding of the underlying mechanisms could greatly enhance the NV centre's effective operation. It is evident that this technique relies on the aforementioned spin polarisation mechanism which is so far only crudely understood. This is reflected by the great variation in reported degrees of polarisation which is a prerequisite for high fidelity initialisation of any qubit. An additional problem is presented

3 Experimentals

by the poor readout contrast (cf. figure 3.4). As a consequence single qubit operations need to be performed several times before the different spin projections can be distinguished. Improvements of the the readout contrast have been recently reported using for example hyperfine coupling with between the NV centre's electron spin and the nuclear spin of the nitrogen atom [61].

3.3 Samples

In our experiments, we used ND samples as well as a bulk sample. Microwave coupling was achieved for both samples by suspending a thin gold wire across the sample. The fundamental differences between nanodiamonds and bulk diamond have been explained in section 2.2. This section describes the specific samples used for conducting the experiments in a more detailed fashion.

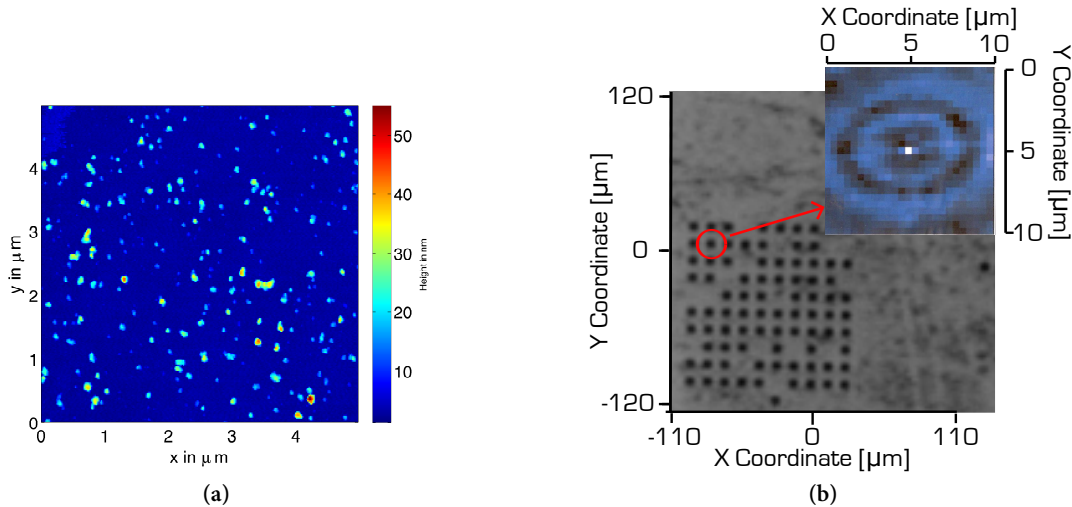


Figure 3.5: (a) Atomic force microscope image of nanodiamonds on a coverslip. (b) Optical microscope image of SILs and fluorescence microscope image of used SIL (red circle).

Nanodiamond samples

The ND samples were fabricated by spincoating a solution of type Ib nanodiamonds and deionised water onto a cover slip. The cover slips were cleaned in an ultrasonic bath using Hellmanex[©](HellmaAnalytics) to remove organic contaminants. We used HPHT type Ib nanodiamonds that are commercially available as polish paste (SYP 0.05 and 0.25, Microdiamant AG). Prior to being spincoated the used nanodiamonds had been centrifuged in order to select for an average size of around 30 nm. An image of a ND sample recorded using an atomic force microscope (AFM) is shown in figure 3.5a.

Bulk sample

The bulk sample used during our experiments was provided by Hannes Bernien and Ronald Hanson from the TU Delft. It is fabricated from a type Ib bulk diamond. Solid immersion lenses (SIL) had been ion-beam milled into the diamond slab with the hope having a single NV centre in the focal area. A suitable NV centre was found to be located in the SIL indicated by the red circle in figure 3.5b. Solid immersion lenses offer an enhanced photon collection by eliminating total internal at the diamond-air interface [62, 63].

4 Results

In this chapter, we present the key experimental results obtained during the course of this master thesis. First, we present results used for identifying single NV centre's and characterising their optical properties. The next two sections explore two level systems in the incoherent and coherent regime. Finally, the results demonstrating the quantum Zeno effect on a single NV centre are presented and discussed.

While the results shown in the first three subsections were obtained for different samples at room as well as cryogenic temperatures, the experiments introduced in the last section were conducted at room temperature on one nanodiamond and on one bulk sample.

4.1 Preliminary characterisation

$g^2(\tau)$ function

As discussed in section 2.3, the $g^{(2)}(\tau)$ functions allow to determine whether the detected fluorescence stems from a single or multiple emitters. To this end, especially when using nanodiamonds $g^{(2)}(\tau)$ functions were recorded (cf. figure 4.1). The observed bunching at medium timescales is a reflection

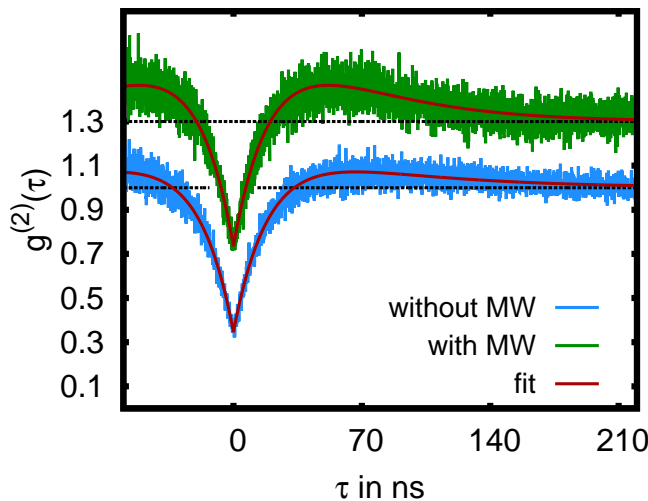


Figure 4.1: $g^{(2)}(\tau)$ function of a single NV centre under continuous MW irradiation and without applied microwave at a constant laser power of $64.5 \mu W$ which was well below the saturation intensity of $340 \mu W$. The green curve has been vertically shifted by 0.3 for better visibility. The solid red curves were obtained by fitting the data to eq. 2.27.

of the existence of the metastable singlet state. This can be explained as follows. After the detection of a photon of a system that had just before been in the metastable state the system will on average undergo several optical cycles before being “trapped” again in the metastable state. Thus the detection

4 Results

of a second photon is more likely compared to long timescales. Here, the occupation probability of the metastable state is not small which leads to a reduced photon emission. This can be illustrated by either comparing $g^{(2)}(\tau)$ functions at different excitation intensities or with and without simultaneous MW-excitation in resonance to a spin transition as is exemplified by figure 4.1. In the latter case, the bunching is more pronounced since the ISC rates are higher for spin 1 states than for spin 0. The obtained data are fitted using formula 2.27.

Saturation of fluorescence

Saturation curves were registered to make sure that the pulses in the following experiments were in the saturated regime, i.e. that short pulses excite the NV centre with high probability.

This was accomplished by attenuating the laser with optical density filters and monitoring the resulting decrease in emitted photons. Plotted in figure 4.2 is the power of the excitation laser I_{exc} versus the detected fluorescence. The data are fitted using the following formula:

$$R(I_{exc}) = \frac{FI_{exc}}{I_{sat} + I_{exc}} \quad (4.1)$$

This formula is derived for a three level system [64] where I_{sat} is the saturation intensity and F the maximal emission rate for $I_{exc} \rightarrow \infty$.

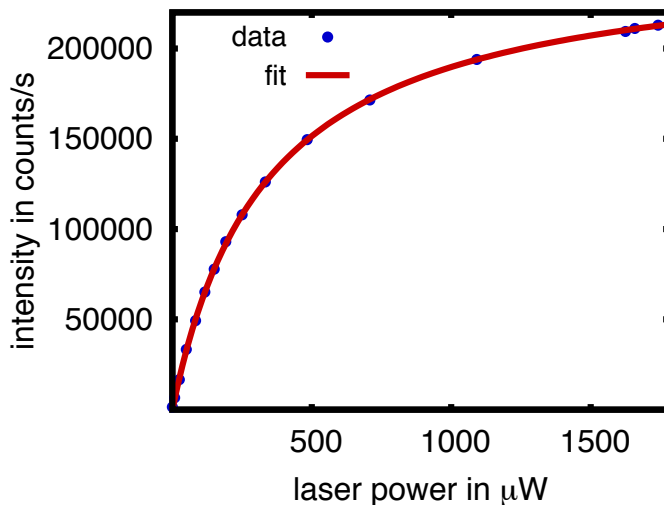


Figure 4.2: Saturation behaviour of the fluorescence emitted by the NV centre in the bulk sample at cryogenic temperatures.

4.2 Incoherent spin manipulation

Incoherent phenomena are observable on time scales τ that are long compared to the relaxation times of the population and coherences, $\tau \gg T_2^*, T_1$. Starting from the stationary solutions of eq. 2.12 one can derive the following expression describing absorption in a two level system

$$\frac{w(\infty, \Delta) - w_0}{w_0} = \frac{(\Delta T_2^*)^2}{1 + (\Delta T_2^*)^2 + T_1 T_2^* \Omega_R^2}. \quad (4.2)$$

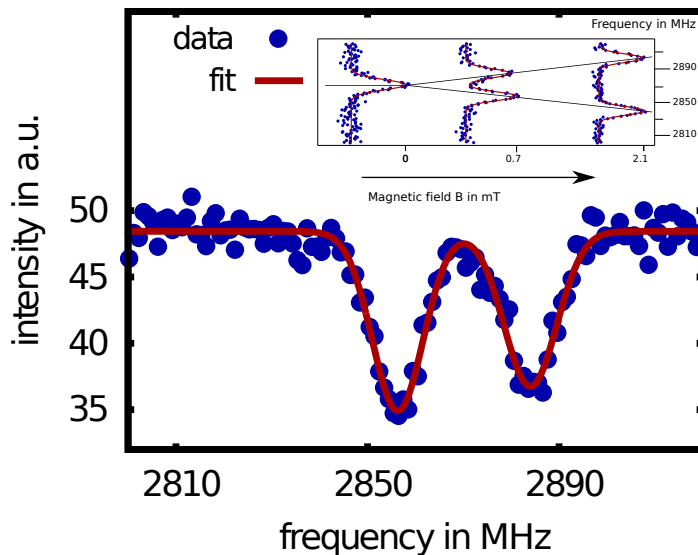


Figure 4.3: Electron spin resonance spectrum for the NV centre in the bulk sample in an external magnetic field. The inset shows the dependence of the splitting on the strength of the static magnetic field. The spectra were recorded with the MW power adjusted to 3 Watt.

The formula describes a Lorentzian and it is noteworthy that in the limit of zero applied field (i.e. $\Omega_R = 0$) the linewidth is determined by the transverse relaxation time T_2^* . Moreover, the term $T_1 T_2^* \Omega_R^2$ leads to the broadening of the absorption profile when the power of the incident field is increased. This broadening being proportional to Ω^2 is widely known as power broadening.

ESR spectra

After verifying that the observed fluorescence was indeed emitted by a single emitter, a MW spectrum was recorded. A magnet was positioned close to the sample to lift the spin degeneracy of the ground state. In order to record the MW spectrum, the magnetic field was kept constant while sweeping the frequency of the microwave. The obtained data is depicted in figure 4.3. When the microwave frequency reaches one of the resonances, the spin state polarisation is changed due to magnetic dipole transitions to the $m_s = \pm 1$ state. Hence a decrease in fluorescence intensity is detected. Depending on angle and distance of the magnet with respect to the sample, the splitting can be adapted to fit the experimental requirements as shown in the inset of figure 4.3

4.3 Coherent manipulation of a single spin

In chapter 2, we briefly introduced the basic theory of two level systems followed by a short exposition of NV centre's properties. In the following part, we report on the experimental realisation of some of the general phenomena observable on a two level system in the coherent regime. During the experiments presented in the remainder of this chapter the splitting between the two $|m_s| = 1$ was adjusted to be greater than 100 MHz. Hence the interaction between the microwave and the NV centre's electron spin can be validly approximated by the theory reviewed in section 2.1.

The experiments were performed by recording the signal over time scales ranging from a few minutes to several hours while performing around 10 000 measurements per second. One should bear in mind that the superposition states observed in the Rabi experiments are not the directly observed

4 Results

superposition of the two spin states but rather probabilities of having found the spin in the upper or lower state via ODMR. The important point is that the measurement of the spin state is an inherently incoherent process which destroys the coherence between the two states. Only by doing the statistics we were able to recover the coherent evolution of the spin.

Rabi oscillations

The resonant interaction of a microwave with a NV centre leads to the coherent superposition of two spin states. This enables us to drive coherent oscillations between the two states. The measured population of $m_s = 0$, i.e. the fluorescence intensity, can be well reproduced by a damped oscillator following

$$f(t) = ae^{-\frac{t}{2T_2^*}} \cos(\Omega t) + c \quad (4.3)$$

where $\Omega = \frac{\mu H}{\hbar}$ denotes the Rabi frequency and T_2^* is the decoherence time. The experimental pulse sequence is shown in figure 4.5b. The green cw laser is switched on for about $5 \mu s$ to prepare the NV centre in the $m_s = 0$ state. A MW driving field was then applied for a varying time, and lastly the laser and photon detector were turned on for optical read-out. Hence, in the experiment we did not directly monitor the continuous evolution of f . Instead, the duration of the microwave is progressively prolonged and f measured. Experimentally detected Rabi oscillations of the NV centre's electron spin are plotted in figure 4.4a. The inset shows the experimental verification of the theoretically expected

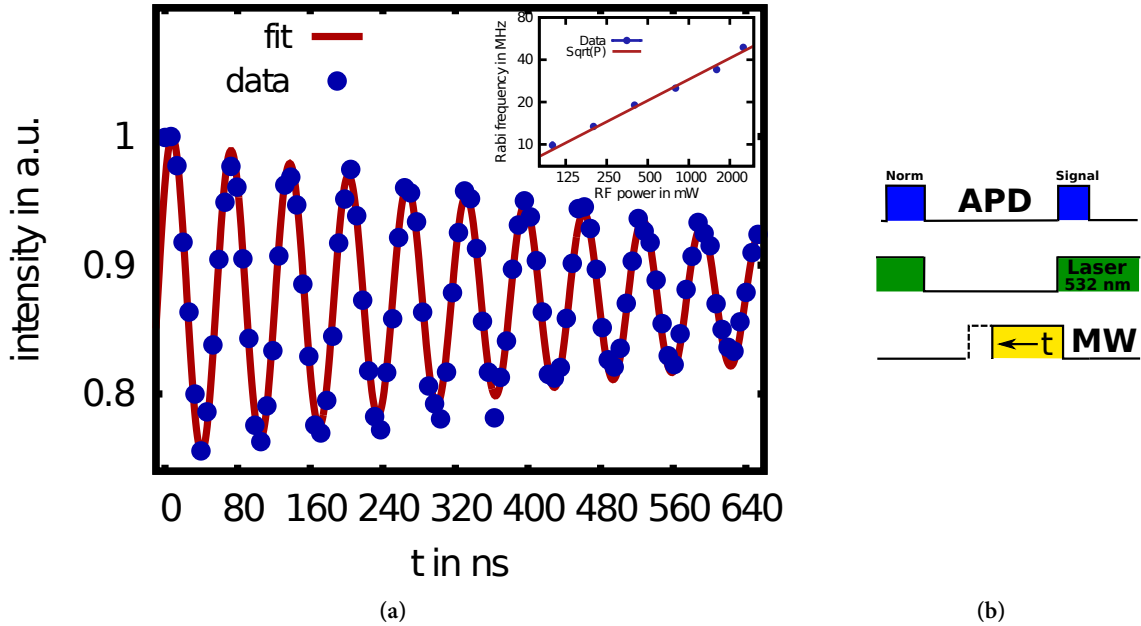


Figure 4.4: (a) Optically detected Rabi oscillations of a single NV electron spin. The data were recorded with the MW and laser power set to 3.2 W and 1.5 mW, respectively. Inset: Rabi frequency as a function of the MW intensity (ln-scale). The solid line represents a square root fit to $\Omega_R(\sqrt{I}) = \frac{d_{12}\sqrt{I}}{\hbar}$. (b) Pulse sequence of the Rabi experiment.

square root dependency of the Rabi frequency on the power of the microwave. Due to incoherent interactions of the NV centre's spin with the environment, the spin dephases with increasing time. The

incoherent interaction are mostly small fluctuations of the magnetic field due to the ^{13}C spin bath in the surroundings of the NV centre [65].

T₁ time

To measure the NV centre's T_1 time we employed the pulse sequence depicted in figure 4.5. The spin is optically initialised then thermalises for a varying time τ . Finally the spin population is optically read out. By consecutively prolonging the time τ , the spin relaxation into the equilibrium state can be retraced. In equilibrium every spin state is populated in average by one third. In figure 4.5a the decay of the fluorescence signal at room temperature of a NV centre prepared in the $m_s = 0$ is depicted. A decrease of the fluorescence is expected for a system initialised in the $m_s = 0$ state. By insertion of an optional π -pulse after state preparation, we initialised the system in $m_s = 1$. Interestingly, here the dynamics of the relaxation processes towards the equilibrium state are significantly faster. In NV centres the spin relaxation time T_1 is very long, on the order of 1-10 ms in bulk samples [66] and on the order of 10 μs -1ms in NDs depending on their respective size and exact position inside of the ND [67]. The investigated T_1 relaxometry is a possible candidate for further applications in magnetic field sensing offering the advantage over T_2 time techniques that it does not necessitate the coherent manipulation of the electron spin. We observed in our experiments T_1 times ranging from 120-260 μs . Hence longitudinal relaxation is negligible compared to the limits posed by the transverse relaxation times in this work which will be discussed in the following section.

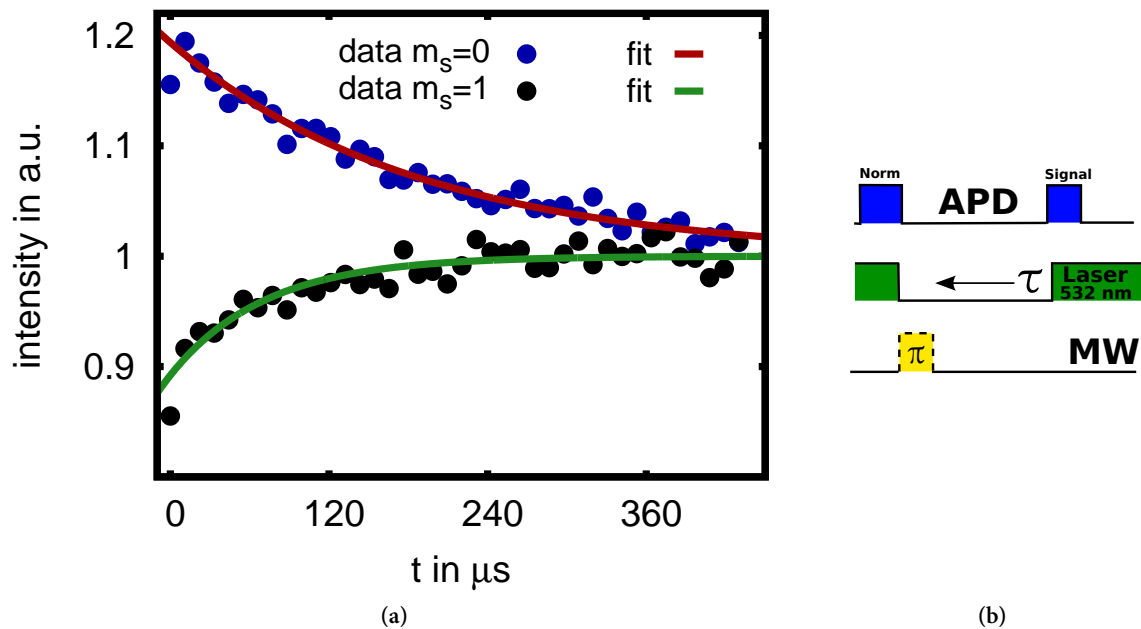


Figure 4.5: (a) Fluorescence signal of a NV centre initially prepared in the $m_s = 0$ (red dots) and $m_s = 1$ (black dots) state at room temperature. The monoexponential fit yielded a decay time of 187,3 μs and 71,6 μs respectively. The laser power measured before the objective lens was 51 μW . (b) Pulse sequence of the T_1 measurement.

Ramsey fringes

One further technique employed in NMR uses the Ramsey sequence depicted in figure 4.6b. The first $\frac{\pi}{2}$ -pulse creates a coherent super-position state in the equatorial plane of the Bloch sphere. During a waiting time of τ the spin is left to freely precess at the frequency determined by the detuning between the field and the transition. Finally, a second $\frac{\pi}{2}$ -pulse maps the accumulated phase into a population. Experimentally recorded Ramsey fringes are shown in figure 4.6a. The Ramsey signal can be fitted to the equation

$$f(t) = ae^{-\left(\frac{t}{T_2^*}\right)^2} \cos(2\pi ft), \quad (4.4)$$

where T_2^* is the transverse relaxation time and f the detuning of the applied field with respect to the spin transition [68]. However, the signal is very noisy and decays very rapidly rendering further analysis questionable. Usually, free electron spin precession experiments allow to determine the T_2^* time [69]. In atomic physics, the sequence is employed to measure the resonance frequency of a transition with very high precision and has accordingly found an important application in atomic clocks [70].

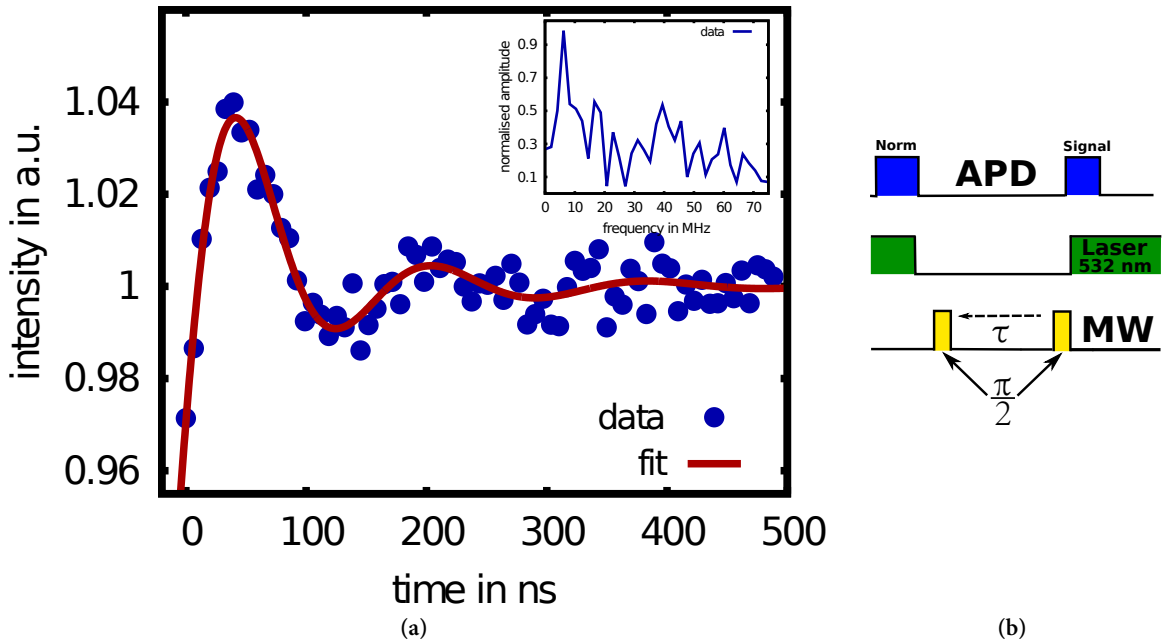


Figure 4.6: (a) Heavily damped Ramsey fringes. The Ramsey signal was fitted to eq. 4.4 obtaining $T_2^*=81.2$ ns. The inset shows the normalised FFT spectrum. The microwave power was adjusted to 2.3 W while the measured laser power was 1.5 mW. (b) Pulse sequence of the Ramsey experiment.

Hahn echo

Spin echo decays are a family of experiments used to determine the decoherence rate of two level systems. The pulse sequence for the experiment is shown in figure 4.7b. Under resonant excitation the first $\frac{\pi}{2}$ -pulse moves the Bloch vector to the equatorial plane. After a certain time τ has elapsed a π -pulse produces a 180° rotation of the Bloch vector within the equatorial plane. After a repeated waiting time of τ the Bloch vector has refocused and the last $\frac{\pi}{2}$ -pulse is used to map the accumulated phase into a detectable population. The decay of the echo now occurs because with increasing τ the phases of

the two state accumulate more and more “random” phase shifts with respect to each other so that the refocusing works less and less. The states are said to *decohere* or *dепhase*. Due to interactions with the ^{13}C spins in the vicinity of the NV centre the length of the T_2 time is extremely sensitive to the angle between the static magnetic field and the NV centre’s quantisation axis [71]. The longest T_2 times are obtained if the field is aligned parallel to the axis of the NV centre [72]. The plot in figure 4.7a shows a typical, experimentally recorded Hahn echo. The Hahn echo decayed with a decoherence time $T_2 = 2,64\mu\text{s}$ obtained by fitting the data to the formula [68]

$$f(t) = Ae^{-\left(\frac{2t}{T_2}\right)^3} + c. \quad (4.5)$$

The inset depicts the corresponding Rabi oscillations with a decoherence time of $T_2^* = 689,29\text{ ns}$. This result exemplifies that photon echoes can be used to preserve quantum coherence. More involved protocols find important applications in quantum information processing and magnetic field sensing offering an even enhanced noise protection [73]. Nevertheless, it is obvious that even by application of echo techniques the observed T_2 times are far smaller than the T_1 times.

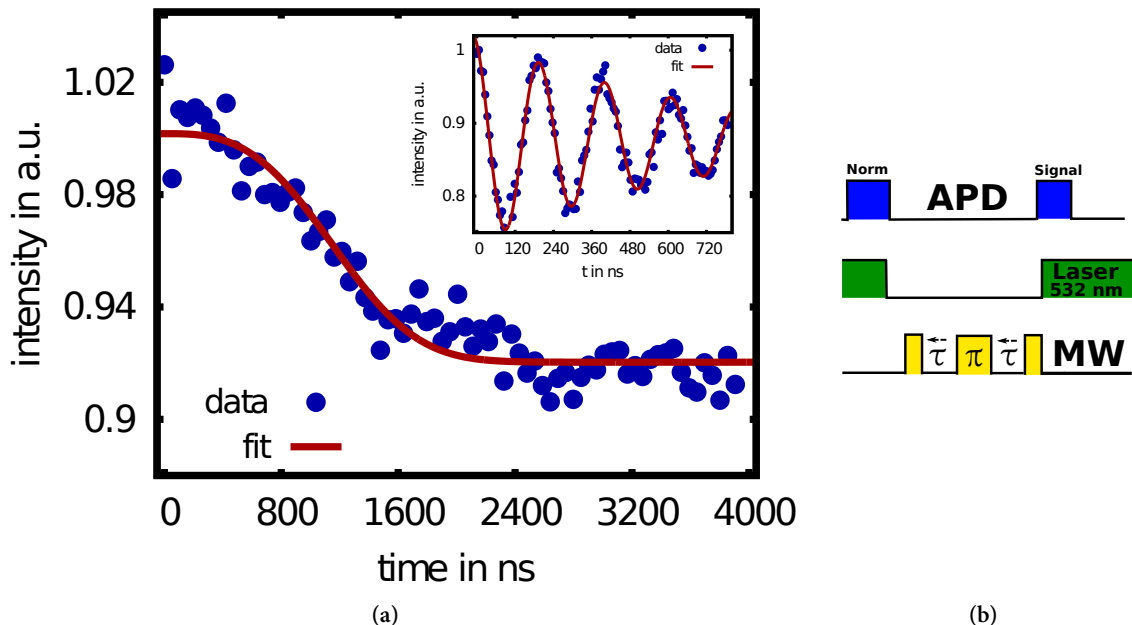


Figure 4.7: (a) Experimentally detected Hahn echo decay. The data were fitted to the function $f(t) \propto e^{-\left(\frac{2t}{T_2}\right)^3}$ yielding $T_2 = 2,64\mu\text{s}$. The inset shows the corresponding Rabi oscillations fading away with a time constant of $T_2^* = 689,29\text{ ns}$. The power of the applied MW was fixed at 2.5 W and the laser power was measured to be 1.2 mW. (b) Pulse sequence of the Hahn echo decay experiment.

4.4 Quantum Zeno effect

In the preceding section, the coherent manipulation of the NV centre’s electronic spin was experimentally shown. The coherence of the spin states however was lost over time due to the incoherent interaction with the environment. Coherence can however also be deliberately destroyed as we show in

4 Results

this section. Here, we revisit the quantum Zeno effect where we use a “measurement” pulse to inhibit the coherent evolution of a system. Cook proposed in his article “What are quantum jumps?” [74] the following experiment to verify the quantum Zeno effect. A three level V-type system as depicted in figure 4.8 is exposed to two fields, each resonant to one transition. The driving field resonant to the $1 \leftrightarrow 2$ transition creates a coherent superposition of the two states. Now, the second field resonant to the $1 \leftrightarrow 3$ transition serves to excite the system from level 1 to level 3. Detection of the resultant fluorescence (or its absence) hence measures in principle the population of the states 1 and 2. If one now performs repeated “measurements” while inducing a transition between 1 and 2 by applying the driving field one can effectively inhibit this transition (cf. section 2.1.3).

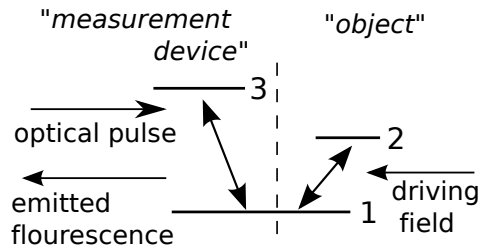


Figure 4.8: Proposed level scheme for testing the QZE

Following the theoretical proposal by *Cook, Itano, Heinzen, Bollinger and Wineland* (IHBW) [75] used around 5000 Be^+ ions confined in a Penning trap to experimentally verify the quantum Zeno effect. The atomic level scheme is shown in figure 4.9 along with the result. They showed that by measuring up to 64 times during the MW pulse, they could almost entirely suppress the transition. It stirred a considerable amount of controversy [29, 30, 76] concerning especially the measurement

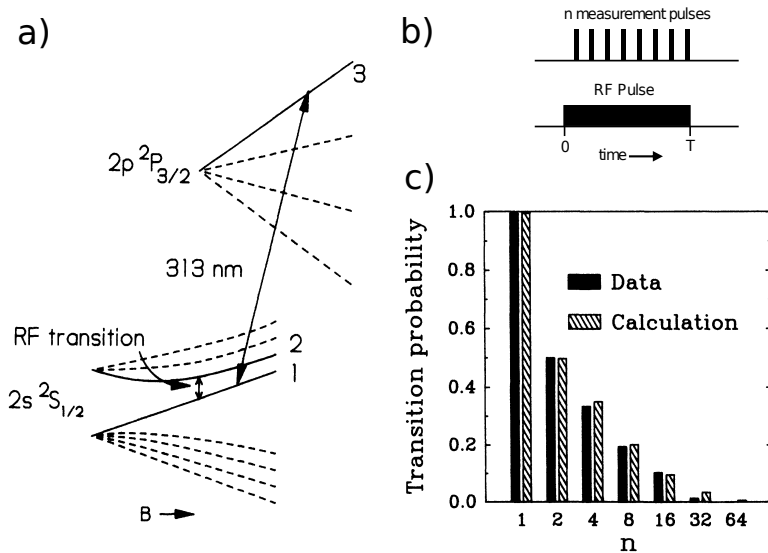
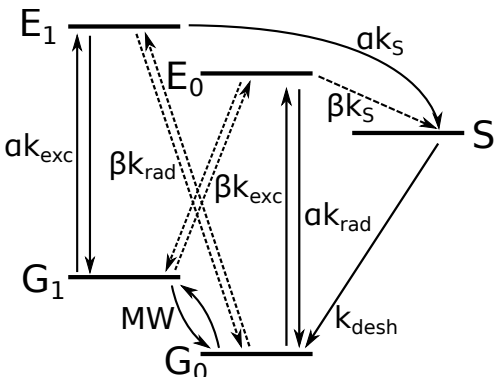


Figure 4.9: a) Level scheme of a Beryllium ion. 1, 2 and 3 correspond to the states mentioned in the main text b) Measurement sequence for the experiment by IHBW c) Experimental results compared to calculated transition probability as a function of n pulses. a) and c) from [75]. b) from [31]

process itself. IHBW did not measure directly the emitted photons (or their absence) resulting from the “projective” laser pulse but rather probed the population of state 1 by applying a readout laser afterwards.

It is however in principle sufficient for the coherence between the two states to be destroyed that the emitted photons are "detected" by the walls of the laboratory. Thus, it represents nowadays the generally accepted experimental proof of the quantum Zeno effect [31, 77].

In analogy to the experiments conducted by IHBW we also attempt to study the inhibition of an induced transition by measurement. Since it had been demonstrated so far only on ensembles we use instead a single solid-state system, namely the electronic spin of the NV centre. However, since the NV centre represents a more complex system compared to the Be^+ ions used by IHBW a few alterations had to be made. First, due to repumping of the optical transition via the metastable state it is not possible to apply repeated optical pulses. This repumping would obscure the Zeno effect. Hence we decided to study the temporal influence of only one single optical pulse with the respect to the applied MW-pulse. Secondly, in order to better understand the experimental results a theoretical model was devised by Janik Wolters to simulate the experiment. The model is explained in more detail in the appendix. The level scheme underlying the model is shown in figure 4.10a. G_0 and G_1 (E_0 and E_1) represent the $m_s = 0$ and $m_s = 1$ level of the ground (excited) state respectively while S designates the metastable singlet state.



(a) Simplified five level scheme of NV centre with relevant transitions

Parameter	Sample	
	ND	Bulk
$2\pi/\Omega$	$80 \pm 0,5 ns$	$240 \pm 7 ns$
$1/k_{exc}$	$33,5 \pm 5 ns$	$30,5 \pm 5 ns$
$1/k_{desh}$	$146 \pm 9 ns$	$220 \pm 60 ns$
θ	$20,1^\circ \pm 1,7^\circ$	$12,4^\circ \pm 3^\circ$
η_{pol}	$0,85 \pm 0,01$	$0,92 \pm 0,01$
T_2^*	$1 \pm 0,5 \mu s$	$0,5 \pm 0,1 \mu s$
$1/k_{rad}$	$34 \pm 5 ns$	$13 \pm 4 ns$
$1/k_s$	$38 \pm 5 ns$	$15,4 \pm 5 ns$
I_{bg}	$0,09 \pm 0,09$	$0,2 \pm 0,1$

(b) Parameters used for simulating the experiment. They were deduced for both samples from independently performed experiments.

Figure 4.10: Simplified level scheme (a) and parameters used for simulating the experiment (b).

In order to optimise the experimental signal, a judicious choice for the pulse sequence used in the experiment is crucial. For this purpose we performed a series of experiments to determine the latency times of the single components in our experiments. The plot in figure 4.11 shows the temporal evolution of the integrated fluorescence during the first microsecond of the optical read-out. For the $m_s = 0$ state (red curve), the fluorescence decreases until the optical steady state is reached. This state has a non-zero population of the singlet state due to the small ISC rate for $m_s = 0$. The dynamics are more complicated for the $m_s = 1$ state (green curve). Here, by shelving in the metastable state the fluorescence decreases up to a minimum at 200 ns. Subsequently, it decays to the steady state within the lifetime of the singlet state ($\tau = 250$ ns). The graph served to determine the optimal timing of the signal gate as well as the exact timing of the microwave. Furthermore, by fitting our model to the data we were able to deduce the transition rates required for simulating our experiment. The other parameters were obtained from experiments described in the preceding sections. The parameters for both samples are

4 Results

listed in table 4.1ob.

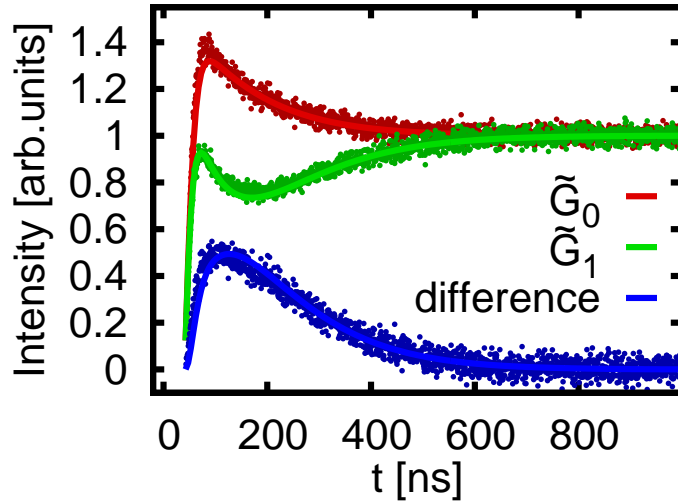


Figure 4.11: Temporal evolution of the integrated fluorescence signal during readout. \tilde{G}_0 and \tilde{G}_1 correspond to $m_s = 0$ and $m_s = 1$, respectively (see text for details). The solid lines represent the fits obtained by fitting the theoretical model to the data. From [78].

We used a ND and a bulk sample for the experiment. The employed pulse sequence is shown in figure 4.12. It can be divided into three parts: initialisation, “measurement” and read-out. The system is prepared in $m_s=0$ by laser illumination. By optional subsequent application of a MW π -pulse the system can also be initialised in $m_s=1$ indicated by the dashed π -pulse. Since the optical initialisation does not polarise the spin with unity fidelity in G_0 (cf. section 3.2) it is written as a superposition state $\tilde{G}_0 = \eta_{pol}G_0 + (1 - \eta_{pol})\exp(i\varphi_1)G_1$ with φ_1 is a random phase. Similarly, a MW π -pulse prepares the state $\tilde{G}_1 = \eta_{pol}G_1 + (1 - \eta_{pol})\exp(i\varphi_2)G_0$. In both cases, η_{pol} represent the achievable spin polarisation (see also figure 4.1ob for an experimentally derived value for η_{pol}).

The following MW π -pulse would then transfer the population to $m_s=1$ ($m_s=0$). This is however the transition that we wish to inhibit. Hence a laser pulse was swept across this MW pulse. Prior to the optical read-out of \tilde{G}_0 a last *optional* MW π -pulse was used to swap the population of the two spin states and effectively read out $m_s=1$.

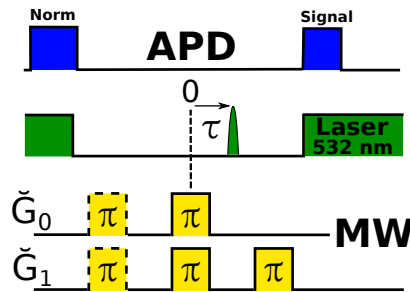


Figure 4.12: Experimental pulse sequence used for conducting the Zeno experiment. \tilde{G}_0 and \tilde{G}_1 refer to the MW pulse sequence used for reading out the respective state.

The experimentally obtained data are plotted in figure 4.13 where figure (a) are the results using

the ND sample and figure (b) for the bulk sample respectively. $\tau=0$ is defined to be the centre of the π -pulse while the dashed vertical lines indicate its end and starting point. On the left of each subfigure is the data obtained without final MW π -pulse hence the state \tilde{G}_0 is read out. For the plot on the right hand side the populations were swapped by the final MW π -pulse and thus \tilde{G}_1 is effectively probed by the read-out laser. The green and red dots represent the data for an initially prepared $m_s=1$ and $m_s=0$ respectively. Another notable difference between the two samples is the difference in the length of the respective MW π -pulse. It was fixed to a length of 40 ns in the ND case and to 120 ns in the case of the bulk diamond. While for the ND sample the laser pulse employed for inhibiting the transition was about 80 ps wide with an energy of roughly 350 pJ, the laser pulse during the bulk sample experiment was 18 ns wide with a peak power of 730 μ W. The laser induces an optical cycle consisting of excitation and subsequent emission of a photon. Like IHBW we don't measure this emitted photon which would in principle allow to determine the state. Instead we optically read out the remaining population of \tilde{G}_0 after the end of the MW π -pulse.

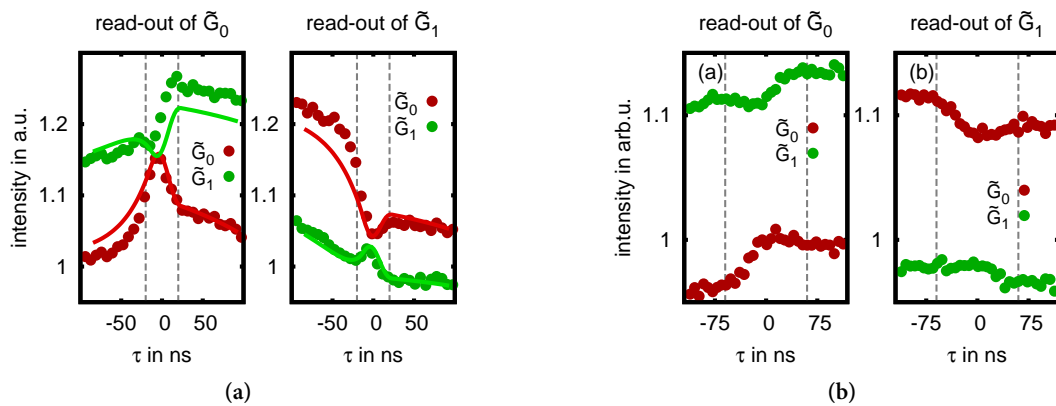


Figure 4.13: Experimental data for the ND (a) and bulk (b) sample. The dashed vertical lines indicate the position of the π -pulse. The red (green) dots represent the data obtained for the NV centre initially prepared in the \tilde{G}_0 (\tilde{G}_1 state). The solid lines in figure (a) are simulations of the experiment.

Discussion

First, we will analyse the results obtained for the ND sample as the data for both samples exhibit very similar behaviour. In addition, the experiment on the bulk sample was chiefly done to preclude that the observed effect arises due to the lifetime of the excited state. Thus, for the experiment using the bulk sample the MW power was adjusted to obtain a π -pulse with the length of 120 ns which is significantly longer than the fluorescence lifetime of ca. 13 ns.

Irrespective of the exact microscopic mechanism which might be phonon coupling, ISC or photon emission and following absorption the microwave induced coherence is destroyed by the strong laser pulse. As is evident from the plots this process depends on the timing of the laser pulse with respect to the applied MW π -pulse with the maximally achievable inhibition at $\tau = 0$. This can be understood by remembering that the coherence between the two states induced by the MW equally reaches its maximum at the centre of a MW π -pulse corresponding to $\tau = 0$. Therefore a laser pulse at $\tau = 0$ effectively hinders the coherent evolution and the final state retains a substantial part of the initial state. For the \tilde{G}_0 state one could object that this behaviour is caused by repolarisation into $m_s = 0$ via ISC. We are able to refute this objection by preparing the system in the $m_s = 1$ state and thus inhibiting the

4 Results

$1 \rightarrow 0$ transition. Here (cf. green dots in figure 4.13), the laser pulse leads to an effective increase in the population of \tilde{G}_1 , an effect that cannot be explained by repolarisation. In order to underpin our analysis further, the experiment was repeated with an additional π -pulse inserted before read-out. This produces an exchange of the populations of the dark and bright state and hence the detected intensity is proportional to the population of \tilde{G}_1 . The experimental data match the previous ones with a maximum inhibition again at the centre of the π -pulse. Moreover, we also calculated the spin projection from the

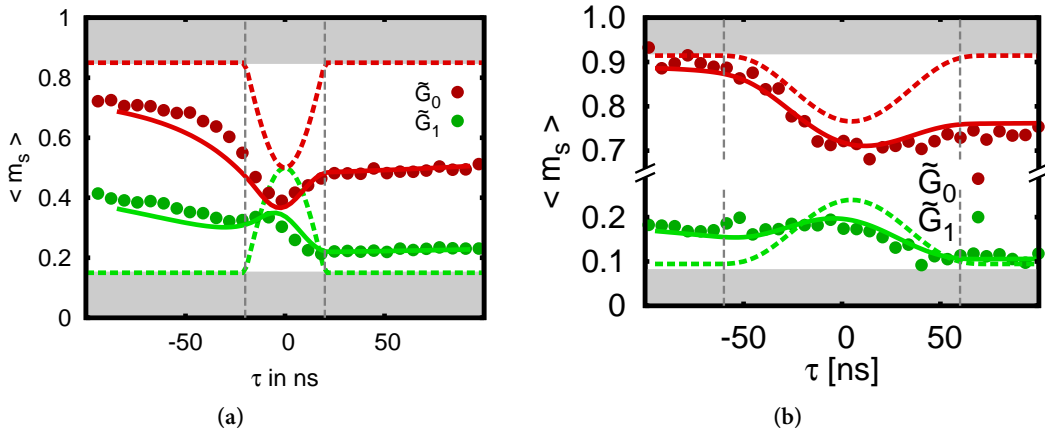


Figure 4.14: Experimental data of the evolution of the spin projections during the experiment for the ND (a) and bulk (b) sample. The solid lines are the results of the simulation while the dashed line represent the ideal Zeno experiment without any relaxation processes. The shaded areas indicate the maximally achievable polarisation

obtained data. The results are plotted for both samples in figure 4.14. The shaded bars in both plots indicate the maximally attainable polarisation of the spins which are 0,85 and 0,92 for the ND and bulk sample respectively. The ideal Zeno experiment is illustrated by the dashed lines in figure 4.14. Here, a laser pulse not within the π -pulse does not affect the population of the two states.

Within the π -pulse the laser pulse suppresses the subsequent coherent evolution between the two states which is most effective at $\tau = 0$ leaving the state in a 50:50 mixture of the two spin states. This however is not directly observed in our case for a number of possible reasons. Firstly, the laser pulse induces some repolarisation due to ISC via the metastable state for states with a large G_1 contribution which are \tilde{G}_1 (\tilde{G}_0) for $\tau < 0$ ($\tau > 0$). Secondly, while for the ND sample the available pulsed laser provided sufficient power to excite the sample with almost unity probability, the AOM-switched cw laser initiates an optical cycle with only 30 % probability. This results in a reduced contrast. Further reasons could be depolarisation via non-spin conserving transitions as mentioned in section 2.2 and the limited T_2^* time bringing about an offset towards 0,5.

Figure 4.15 shows the same experimental data as figure 4.14. This time however, the dashed line indicates a simulation during which coherences in the excited state were artificially introduced while leaving all other effects unaltered. This effectively turns off the QZE. Evidently, in figure 4.15a the difference is not very pronounced. Additional simulations showed (see appendix for more details) that in particular the lifetime of the excited state was deleterious to observing the QZE. This was the reason why we decided to repeat the experiment using the bulk sample and adjusting the π -pulses to be significantly longer than the lifetime of the excited state. Here, in figure 4.15b, the deviations between the simulation and the experimental data are clearly visible at $\tau = 0$. This further indicates that in

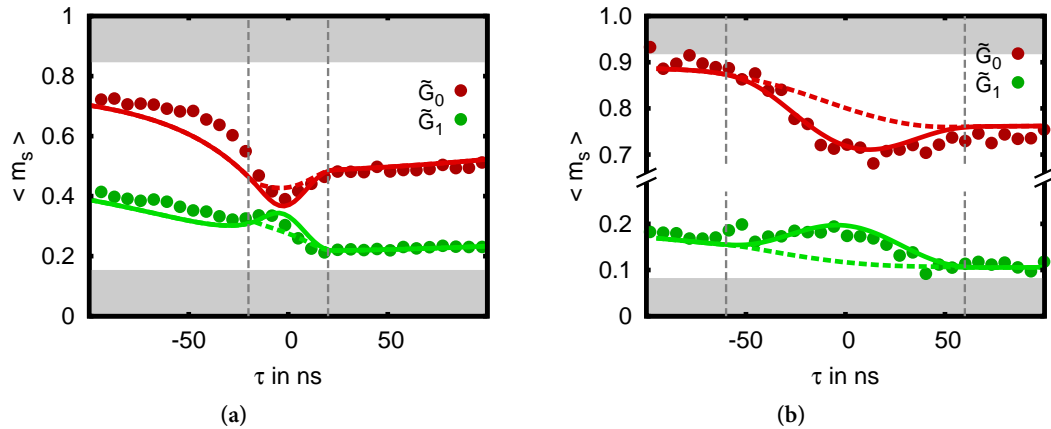


Figure 4.15: Experimental data of the evolution of the spin projections during the experiment for the ND (a) and bulk (b) sample. The solid lines are the results of the simulation taking all effects into account while the dashed line represent the modelled experiment where the Zeno effect is effectively turned off (see main text for more details). The shaded areas indicate the maximally achievable polarization

our experiments the laser pulse effectively initiates the measurement of the spin state and hence the coherences between the two spin states are destroyed.

5 Conclusion & outlook

Nowadays, the coherent manipulation of the NV centre's electronic spin is a well established technique and a number of quantum optical hallmark experiments have been performed on it such as the Hong-Ou-Mandel effect [37] and entanglement between two electronic spins [51].

We implemented some of the basic experiments such as Rabi oscillations and spin echos. These experiments have been conducted at room and cryogenic temperatures using nanodiamond samples as well as a bulk sample. With our experiments we aimed at substantiating another purely quantum mechanical phenomenon, the quantum Zeno effect. This can be understood as the limiting case of measurement induced strong decoherence. We studied the temporal influence of the "measurement" pulse with respect to the coherence inducing MW pulse. Our experiments showed that the coherent evolution of the NV centre's electron spin could indeed be inhibited. The experimental findings were also well reproduced by the theoretical model which helped to identify the different contributions to the observed phenomenon. A ND represents thus a single quantum system whose dynamics are thoroughly characterised with respect to coherent as well as incoherent processes. These insights might help to improve the understanding of the ND's interaction with its mesoscopic environments in experiments where it is used as a scanning quantum emitter probe.

Additional studies could consist in repeating the experiment at cryogenic temperatures with better suited diamond samples. This would enable resonant, spin selective optical excitation. Together with the longer decoherence times this would not only render the observed effects more pronounced but also repeated measurements might be feasible due to low ISC rates from the excited state $m_s = 0$ manifold.

A Theoretical supplement

NV model system

In this section the theoretical model used for simulating the experiment is explained in more detail. Since the splitting between $m_s=1$ and $m_s=-1$ induced by the static magnetic field was adjusted to be greater than 250 MHz (which is far greater than the spectral width of the applied rf-field (FWHM < 6 Hz in cw operation)) we can safely neglect $m_s=-1$. The excited state fine structure (cf. section 2.2) is also simplified and only retain $m_s=0$ and $m_s=1$. The two metastable states are also combined to one. The spin mixing which is chiefly induced by strain is accounted for by introducing α and β . These allow for spin non-conserving transitions and are both correlated via the phenomenological spin mixing angle ϑ .

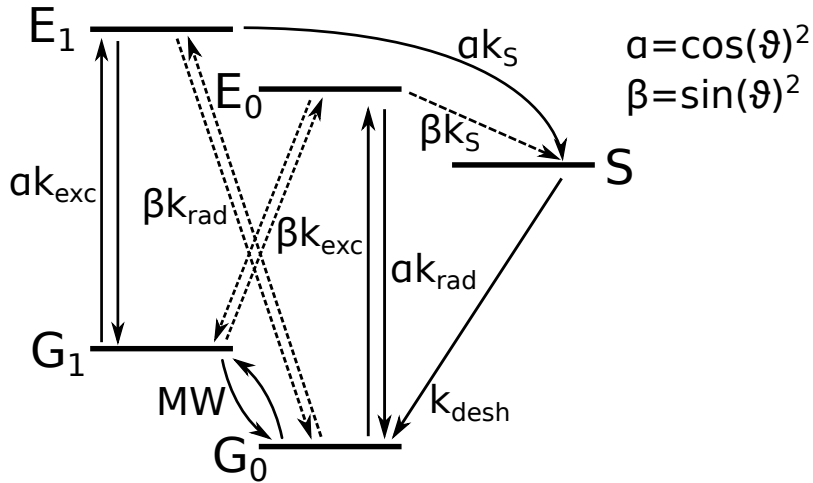


Figure A.1: Level scheme used for simulating the experiment

The transitions between the spin ground states $G_0(t)$ and $G_1(t)$ are described completely quantum mechanically while for the other transitions the coherences between the states are neglected and hence are modelled using rate equations.

We assume that quantum coherences are lost during excitation while in reality they might be lost during decay. $\Omega(t)$ is the time dependent MW Rabi frequency. The equations can be written as an algebraic equation

$$\frac{d}{dt}x = Ax \quad (\text{A.1})$$

with

$$x = \begin{pmatrix} G_0 \\ G_1 \\ \Im\{C_{01}\} \\ E_0 \\ E_1 \\ S \end{pmatrix} \quad \text{and} \quad A = \begin{pmatrix} -k_{exc} & 0 & -\Omega & \alpha k_{rad} & \beta k_{rad} & k_{desh} \\ 0 & -k_{exc} & \Omega & \beta k_{rad} & \alpha k_{rad} & 0 \\ \frac{i\Omega}{2} & \frac{-i\Omega}{2} & \Gamma & 0 & 0 & 0 \\ \alpha k_{exc} & \alpha k_{exc} & 0 & -k_{rad} & 0 & \beta k_S \\ \beta k_{exc} & \beta k_{exc} & 0 & -k_{rad} & 0 & \alpha k_S \\ 0 & 0 & 0 & \beta k_S & \alpha k_S & -k_{desh} \end{pmatrix}$$

and $\Gamma = -(1/T_2^* + k_{exc})$. All the entries of x designate the respective level populations apart from $\Im\{C_{01}\}$ which is the imaginary part of the coherence between G_0 and G_1 .

In figures A.2 and figure A.3, we used simulations of the Zeno experiments (whose data is shown in figure 4.14) to artificially turn off certain transition in the model. These simulations allow to identify the respective contributions of the different processes to the experimentally recorded data.

Figure A.2 shows the simulation of the experiment using the bulk sample. Evidently, repumping via ISC is responsible for most of the observed deviation between the experiment and the ideal Zeno experiment (cf. figure 4.14b) while the lifetime of the excited state contributes little.

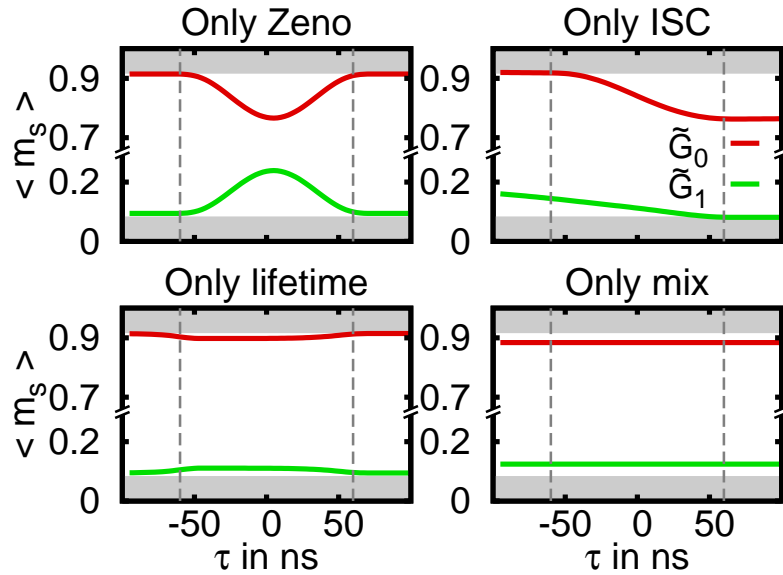


Figure A.2: Detailed analysis of the influence of the Zeno effect, repumping by ISC, the finite life time of the excited state and level mixing on the m_s spin projection in the bulk experiment when initially preparing \tilde{G}_0 (\tilde{G}_1). For each individual plot all remaining competing effects were switched off. For the Zeno effect, this was achieved by introducing excited state coherences and assuming that neither excitation nor decay lead to dephasing.

Figure A.3 shows the simulation of the experiment using the ND sample. Here, it is also repumping via ISC that contributes substantially to the observed deviation between the experiment and the ideal Zeno experiment (cf. figure 4.14a). More interesting is however that the lifetime of the excited state has a much more pronounced effect which helps to explain the only slight deviation between the two simulations in figure 4.15a.

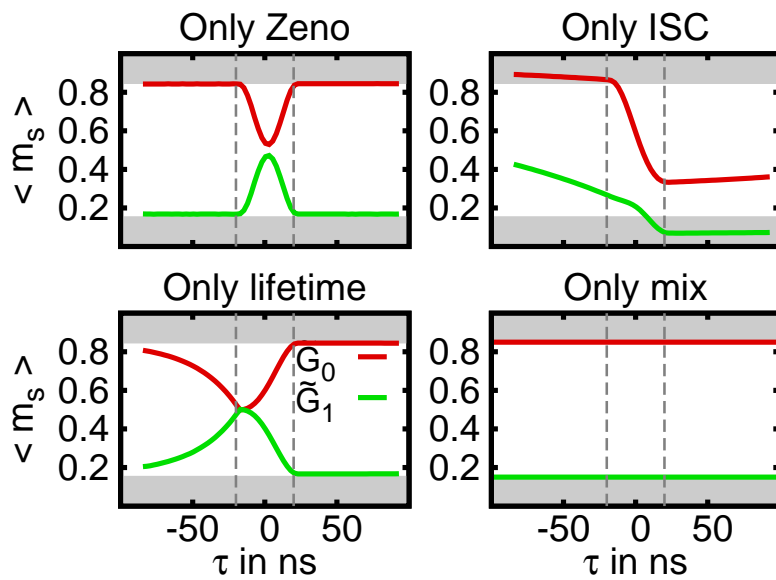


Figure A.3: Detailed analysis of the influence of the Zeno effect, repumping by ISC, the finite life time of the excited state and level mixing on the m_s spin projection in the ND experiment when initially preparing \tilde{G}_0 (\tilde{G}_1). For each individual plot all remaining competing effects were switched off. For the Zeno effect, this was achieved by introducing excited state coherences and assuming that neither excitation nor decay lead to dephasing.

Bibliography

- [1] TS Kuhn. *The structure of scientific revolutions*. The University of Chicago Press, 1996.
- [2] Richard P. Feynman. ‘Simulating physics with computers’. In: *International Journal of Theoretical Physics* 21.6-7 (June 1982), pp. 467–488. DOI: 10.1007/BF02650179.
- [3] T D Ladd et al. ‘Quantum computers.’ In: *Nature* 464.7285 (Mar. 2010), pp. 45–53. DOI: 10.1038/nature08812.
- [4] Jörg Wrachtrup and Fedor Jelezko. *Processing quantum information in diamond*. May 2006. DOI: 10.1088/0953-8984/18/21/S08.
- [5] Jianming Cai et al. ‘A large-scale quantum simulator on a diamond surface at room temperature’. In: *Nature Physics* 9.3 (Jan. 2013), pp. 168–173. DOI: 10.1038/nphys2519.
- [6] K. D. Jahnke et al. ‘Long coherence time of spin qubits in ¹²C enriched polycrystalline chemical vapor deposition diamond’. In: *Applied Physics Letters* 101.1 (2012), p. 012405. DOI: 10.1063/1.4731778.
- [7] F. Jelezko et al. ‘Observation of Coherent Oscillations in a Single Electron Spin’. In: *Physical Review Letters* 92.7 (Feb. 2004), pp. 1–4. DOI: 10.1103/PhysRevLett.92.076401.
- [8] H. Bernien et al. ‘Heralded entanglement between solid-state qubits separated by three metres’. In: *Nature* (Apr. 2013). DOI: 10.1038/nature12016.
- [9] TA Kennedy and FT Charnock. ‘Single-Qubit Operations with the Nitrogen-Vacancy Center in Diamond’. In: *... status solidi (b)* 426.3 (2002), pp. 416–426.
- [10] G. Waldherr et al. ‘Violation of a Temporal Bell Inequality for Single Spins in a Diamond Defect Center’. In: *Physical Review Letters* 107.9 (Aug. 2011), p. 090401. DOI: 10.1103/PhysRevLett.107.090401.
- [11] N Mohan et al. ‘In vivo imaging and toxicity assessments of fluorescent nanodiamonds in *Caenorhabditis elegans*’. In: *Nano letters* (2010).
- [12] G Kucsko et al. ‘Nanometre-scale thermometry in a living cell.’ In: *Nature* 500.7460 (Aug. 2013), pp. 54–8. DOI: 10.1038/nature12373.
- [13] F. Dolde et al. ‘Electric-field sensing using single diamond spins’. In: *Nature Physics* 7.6 (Apr. 2011), pp. 459–463. DOI: 10.1038/nphys1969.
- [14] G. de Lange et al. ‘Single-Spin Magnetometry with Multipulse Sensing Sequences’. In: *Physical Review Letters* 106.8 (Feb. 2011), p. 080802. DOI: 10.1103/PhysRevLett.106.080802.
- [15] AW Schell, P Engel, and O Benson. ‘Probing the local density of states in three dimensions with a scanning single quantum emitter’. In: *arXiv preprint arXiv:1303.0814* (2013).
- [16] Aristotle. *Aristotle’s Physics*. Ed. by W. D. Ross. Oxford University Press, 1936.
- [17] B. Misra and E. C. G. Sudarshan. ‘The Zeno’s paradox in quantum theory’. In: *Journal of Mathematical Physics* 18.4 (1977), p. 756. DOI: 10.1063/1.523304.
- [18] F Bloch, WW Hansen, and M Packard. ‘Nuclear induction’. In: *Physical review* 652.1938 (1946).

Bibliography

- [19] LC Allen and JH Eberly. *Optical resonance and two-level atoms*. Dover, 1975.
- [20] C Cohen-Tannoudji and J Dupont-Roc. *Atom-Photon Interactions: Basic Processes and Applications*. WILEY-VCH Verlag, 2004.
- [21] Christopher J. Foot. *Atomic Physics*. Oxford University Press, 2005.
- [22] G D Fuchs et al. ‘Gigahertz dynamics of a strongly driven single quantum spin.’ In: *Science (New York, N.Y.)* 326.5959 (Dec. 2009), pp. 1520–2. DOI: 10.1126/science.1181193.
- [23] Richard P. Feynman, Frank L. Vernon, and Robert W. Hellwarth. ‘Geometrical Representation of the Schrödinger Equation for Solving Maser Problems’. In: *Journal of Applied Physics* 28.1 (1957), p. 49. DOI: 10.1063/1.1722572.
- [24] II Rabi. ‘Space quantization in a gyrating magnetic field’. In: *Physical Review* 51.1931 (1937).
- [25] HC Torrey. ‘Transient Nutations in Nuclear Magnetic Resonance’. In: *Physical Review* 76.8 (1949).
- [26] Daniel Greenberger, Klaus Hentschel, and Friedel Weinert. *Compendium of Quantum Physics: Concepts, Experiments, History and Philosophy*. 2009, pp. XVI, 901. DOI: 10.1007/978-3-540-70626-7.
- [27] Charles Santori, David Fattal, and Yoshihisa Yamamoto. *Single-photon Devices and Applications*. WILEY-VCH Verlag, 2010.
- [28] Wojciech Hubert Zurek. ‘Decoherence, einselection, and the quantum origins of the classical’. In: *Reviews of Modern Physics* 75.3 (May 2003), pp. 715–775. DOI: 10.1103/RevModPhys.75.715.
- [29] LE Ballentine. ‘Comment on “quantum zeno effect”’. In: *Physical Review A* 43.9 (1991), pp. 5165–5167.
- [30] WM Itano and DJ Heinzen. ‘Reply to“Comment on Quantum Zeno effect”’. In: *Physical Review* ... (1991).
- [31] WM Itano. ‘Perspectives on the quantum Zeno paradox’. In: *Journal of Physics: Conference Series* (2009). arXiv:0612187v1 [arXiv:quant-ph].
- [32] A. Zaitsev. ‘Vibronic spectra of impurity-related optical centers in diamond’. In: *Physical Review B* 61.19 (May 2000), pp. 12909–12922. DOI: 10.1103/PhysRevB.61.12909.
- [33] I Aharonovich et al. ‘Diamond-based single-photon emitters’. In: *Reports on Progress in Physics* 74.7 (July 2011), p. 076501. DOI: 10.1088/0034-4885/74/7/076501.
- [34] M. Doherty et al. ‘Theory of the ground-state spin of the NV⁻ center in diamond’. In: *Physical Review B* 85.20 (May 2012), p. 205203. DOI: 10.1103/PhysRevB.85.205203.
- [35] L Robledo et al. ‘Control and coherence of the optical transition of single nitrogen vacancy centers in diamond’. In: *Physical review letters* (2010).
- [36] Janik Wolters et al. ‘Measurement of the Ultrafast Spectral Diffusion of the Optical Transition of Nitrogen Vacancy Centers in Nano-Size Diamond Using Correlation Interferometry’. In: *Physical Review Letters* 110.2 (Jan. 2013), p. 027401. DOI: 10.1103/PhysRevLett.110.027401.
- [37] Hannes Bernien et al. ‘Two-Photon Quantum Interference from Separate Nitrogen Vacancy Centers in Diamond’. In: *Physical Review Letters* 108.4 (Jan. 2012), p. 043604. DOI: 10.1103/PhysRevLett.108.043604.
- [38] C Kurtsiefer et al. ‘Stable solid-state source of single photons’. In: *Physical review letters* 85.2 (July 2000), pp. 290–3.

- [39] Roland Albrecht et al. ‘Coupling of a Single Nitrogen-Vacancy Center in Diamond to a Fiber-Based Microcavity’. In: *Physical Review Letters* 110.24 (June 2013), p. 243602. DOI: 10.1103/PhysRevLett.110.243602.
- [40] Igor Aharonovich, Andrew D. Greentree, and Steven Prawer. ‘Diamond photonics’. In: *Nature Photonics* 5.7 (June 2011), pp. 397–405. DOI: 10.1038/nphoton.2011.54.
- [41] F. Jelezko and J. Wrachtrup. ‘Single defect centres in diamond: A review’. In: *Physica Status Solidi (a)* 203.13 (Oct. 2006), pp. 3207–3225. DOI: 10.1002/pssa.200671403.
- [42] Florian Hilser and Guido Burkard. ‘All-optical control of the spin state in the NV⁻ center in diamond’. In: *Physical Review B* 86.12 (Sept. 2012), p. 125204. DOI: 10.1103/PhysRevB.86.125204.
- [43] V. M. Acosta et al. ‘Temperature Dependence of the Nitrogen-Vacancy Magnetic Resonance in Diamond’. In: *Physical Review Letters* 104.7 (Feb. 2010), p. 070801. DOI: 10.1103/PhysRevLett.104.070801.
- [44] J R Maze et al. ‘Properties of nitrogen-vacancy centers in diamond: the group theoretic approach’. In: *New Journal of Physics* 13.2 (Feb. 2011), p. 025025. DOI: 10.1088/1367-2630/13/2/025025.
- [45] Ph Tamarat et al. ‘Spin-flip and spin-conserving optical transitions of the nitrogen-vacancy centre in diamond’. In: *New Journal of Physics* 10.4 (Apr. 2008), p. 045004. DOI: 10.1088/1367-2630/10/4/045004.
- [46] A. Batalov et al. ‘Low Temperature Studies of the Excited-State Structure of Negatively Charged Nitrogen-Vacancy Color Centers in Diamond’. In: *Physical Review Letters* 102.19 (May 2009), p. 195506. DOI: 10.1103/PhysRevLett.102.195506.
- [47] E Togan et al. ‘Quantum entanglement between an optical photon and a solid-state spin qubit.’ In: *Nature* 466.7307 (Aug. 2010), pp. 730–4. DOI: 10.1038/nature09256.
- [48] G. D. Fuchs et al. ‘Spin Coherence during Optical Excitation of a Single Nitrogen-Vacancy Center in Diamond’. In: *Physical Review Letters* 108.15 (Apr. 2012), p. 157602. DOI: 10.1103/PhysRevLett.108.157602.
- [49] A.J. Neves and M.H. Nazaré. *Properties, growth, and applications of diamond*. INSPEC, The Institution of Electrical Engineers, 2001.
- [50] Gopalakrishnan Balasubramanian et al. ‘Ultralong spin coherence time in isotopically engineered diamond.’ In: *Nature materials* 8.5 (May 2009), pp. 383–7. DOI: 10.1038/nmat2420.
- [51] F Dolde et al. ‘Room-temperature entanglement between single defect spins in diamond’. In: *Nature Physics* 8.2 (2013), pp. 1–5. DOI: 10.1038/nphys2545.
- [52] Oliver Benson. ‘Assembly of hybrid photonic architectures from nanophotonic constituents.’ In: *Nature* 480.7376 (Dec. 2011), pp. 193–9. DOI: 10.1038/nature10610.
- [53] L P McGuinness et al. ‘Quantum measurement and orientation tracking of fluorescent nanodiamonds inside living cells.’ In: *Nature nanotechnology* 6.6 (June 2011), pp. 358–63. DOI: 10.1038/nnano.2011.64.
- [54] Liam T Hall et al. ‘Monitoring ion-channel function in real time through quantum decoherence.’ In: *Proceedings of the National Academy of Sciences of the United States of America* 107.44 (Nov. 2010), pp. 18777–82. DOI: 10.1073/pnas.1002562107.
- [55] L Mandel and E Wolf. *Optical coherence and quantum optics*. Cambridge University Press, 1995.
- [56] D Meschede. *Optics, light and lasers*. WILEY-VCH Verlag, 2004.

Bibliography

- [57] Fedor Jelezko. ‘Defekte mit Effekt’. In: *Physik Journal* 7.8 (2008), pp. 63–68.
- [58] J Wrachtrup, C Von Borczyskowski, and J Bernard. ‘Optical detection of magnetic resonance in a single molecule’. In: *Nature* 363 (1993), pp. 244–245.
- [59] Marcus W Doherty et al. ‘The nitrogen-vacancy colour centre in diamond’. In: (2013), pp. 1–101. arXiv:arXiv:1302.3288v1.
- [60] A P Nizovtsev et al. ‘A Quantum Computer Based on NV Centers in Diamond : Optically Detected Nutations of Single Electron and Nuclear Spins’. In: *Optics and ...* 99.2 (2005), pp. 233–244.
- [61] M. Steiner et al. ‘Universal enhancement of the optical readout fidelity of single electron spins at nitrogen-vacancy centers in diamond’. In: *Physical Review B* 81.3 (Jan. 2010), p. 035205. DOI: 10.1103/PhysRevB.81.035205.
- [62] J. P. Hadden et al. ‘Strongly enhanced photon collection from diamond defect centers under microfabricated integrated solid immersion lenses’. In: *Applied Physics Letters* 97.24 (2010), p. 241901. DOI: 10.1063/1.3519847.
- [63] P Siyushev et al. ‘Monolithic diamond optics for single photon detection.’ In: *Applied physics letters* 97.24 (Dec. 2010), p. 241902. DOI: 10.1063/1.3519849.
- [64] Stefan Schietinger. ‘Investigation ,Manipulation and Coupling of Single Nanoscopic and Quantum Emitters’. PhD thesis. Humboldt Universität zu Berlin, 2012.
- [65] Boris Naydenov et al. ‘Dynamical decoupling of a single-electron spin at room temperature’. In: *Physical Review B* 83 (2011), p. 4. DOI: 10.1103/PhysRevB.83.081201. arXiv:1008.1953.
- [66] A. Jarmola et al. ‘Temperature- and Magnetic-Field-Dependent Longitudinal Spin Relaxation in Nitrogen-Vacancy Ensembles in Diamond’. In: *Physical Review Letters* 108.19 (May 2012), p. 197601. DOI: 10.1103/PhysRevLett.108.197601.
- [67] J.-P. Tetienne et al. ‘Spin relaxometry of single nitrogen-vacancy defects in diamond nanocrystals for magnetic noise sensing’. In: *Physical Review B* 87.23 (June 2013), p. 235436. DOI: 10.1103/PhysRevB.87.235436.
- [68] G de Lange et al. ‘Universal dynamical decoupling of a single solid-state spin from a spin bath.’ In: *Science (New York, N.Y.)* 330.6000 (Oct. 2010), pp. 60–3. DOI: 10.1126/science.1192739.
- [69] L Childress et al. ‘Coherent dynamics of coupled electron and nuclear spin qubits in diamond.’ In: *Science (New York, N.Y.)* 314.5797 (Oct. 2006), pp. 281–5. DOI: 10.1126/science.1131871.
- [70] G Grynberg, A Aspect, and C Fabre. *Introduction to Quantum Optics*. Cambridge University Press, 2010.
- [71] J. Maze, J. Taylor, and M. Lukin. ‘Electron spin decoherence of single nitrogen-vacancy defects in diamond’. In: *Physical Review B* 78.9 (Sept. 2008), p. 094303. DOI: 10.1103/PhysRevB.78.094303.
- [72] P. L. Stanwix et al. ‘Coherence of nitrogen-vacancy electronic spin ensembles in diamond’. In: *Physical Review B* 82.20 (Nov. 2010), p. 201201. DOI: 10.1103/PhysRevB.82.201201.
- [73] Gang-Qin Liu et al. ‘Noise-resilient quantum evolution steered by dynamical decoupling.’ In: *Nature communications* 4 (Aug. 2013), p. 2254. DOI: 10.1038/ncomms3254.
- [74] Richard J Cook. ‘What are Quantum Jumps?’ In: *Physica Scripta* T21 (Jan. 1988), pp. 49–51. DOI: 10.1088/0031-8949/1988/T21/009.
- [75] Wayne M WM Itano et al. ‘Quantum Zeno Effect’. In: *Phys. Rev. A* 41.5 (1990), p. 2295.

- [76] Hiromichi Nakazato et al. ‘Understanding the quantum Zeno effect’. In: *Physics Letters A* 217.July (1996), pp. 203–208.
- [77] P. Facchi, H. Nakazato, and S. Pascazio. ‘From the Quantum Zeno to the Inverse Quantum Zeno Effect’. In: *Physical Review Letters* 86.13 (Mar. 2001), pp. 2699–2703. DOI: 10.1103/PhysRevLett.86.2699.
- [78] Janik Wolters et al. ‘Quantum Zeno phenomenon on a single solid-state spin’. In: *Physical Review A* 88.2 (Aug. 2013), p. 020101. DOI: 10.1103/PhysRevA.88.020101.

List of Figures

1.1 Representation of a qubit on the Bloch sphere	1
1.2 Illustration of the experiment.	2
2.1 Scheme of two level system.	3
2.2 The Bloch vector of a pure state on the Bloch sphere.	4
2.3 Calculated Rabi oscillations.	6
2.4 Crystallographic model of the NV centre	9
2.5 Fluorescence spectrum	10
2.6 Level scheme of the NV centre	11
2.7 $g^{(2)}(t)$ functions	13
3.1 Experimental setup	16
3.2 (a) Sketch of a confocal microscope. (b) Sketch of a HBT interferometer.	18
3.3 (a) Simplified level scheme of NV centre with relevant transitions. (b) Fluorescence decay of a NV centre initially prepared in the $m_s = 0$ and $m_s = 1$ state in a bulk sample, respectively.	18
3.4 General measurement protocol	19
3.5 (a) Atomic force microscope image of nanodiamonds on a coverslip. (b) Optical microscope image of SILs and fluorescence microscope image of used SIL (red circle).	20
4.1 $g^{(2)}(\tau)$ function of a single NV centre	21
4.2 Saturation of NV fluorescence	22
4.3 ESR spectrum	23
4.4 Rabi experiment	24
4.5 T1 time experiment	25
4.6 Ramsey experiment	26
4.7 Hahn echo decay experiment	27
4.8 Proposed level scheme for testing the QZE	28
4.9 IHBW results	28
4.10 Simplified level scheme (a) and parameters used for simulating the experiment (b).	29
4.11 Fluorescence during readout	30
4.12 Pulse sequence for Zeno experiment	30
4.13 Experimental data of the Zeno experiment	31
4.14 Spin projection and ideal Zeno experiment	32
4.15 Spin projection and switched-off Zeno effect	33
A.1 Level scheme used for theoretical model	37
A.2 Theoretical analysis of bulk experiment	38
A.3 Theoretical analysis of ND experiment	39

Own Publications

Publications

'Quantum Zeno phenomenon on a single solid-state spin'

J. Wolters, M. Strauß, R. S. Schoenfeld, and O. Benson, Physical Review A 88, 020101 (2013).

Conference contributions

Talks

DPG Frühjahrstagung Hannover, 2013

Max Strauß, Janik Wolters, Niko Nikolay, Simon Schönenfeld, Oliver Benson

'Observing the quantum Zeno effect on a single solid state spin'

Poster

519. WE-Heraeus-Seminar HYBRID QUANTUM SYSTEMS, 2012

Max Strauß, Niko Nikolay, Janik Wolters, Oliver Benson

'Coherent manipulation of a single solid state spin'

Selbständigkeitserklärung

Hiermit erkläre ich, dass ich die vorliegende Arbeit selbständig und nur unter Verwendung der angegebenen Literatur und Hilfsmittel angefertigt habe.

Berlin, den 10. November 2013

Stefan Maximilian Strauß